Experiments in Fluids (2021) 62:152
https://doi.org/10.1007/s00348-021-03239-y

RESEARCH ARTICLE

Aerofoil self-noise radiations subjected to serration flap angles

P. C. Woodhead[1] · T. P. Chong[1] · P. F. Joseph[2] · A. Vathylakis[1]

Received: 27 January 2021 / Revised: 5 June 2021 / Accepted: 8 June 2021

Abstract

Besides the investigation of the aeroacoustics responses of an asymmetric aerofoil subjected to serrated trailing edge flap angles from negative (flap-down) to positive (flap-up), this paper also provides a new perspective on the physical mechanisms of broadband noise reduction by a serrated trailing edge. The blade-loading effect, which is a function of the length and flap angle for a straight/non-serrated trailing edge flat plate, plays a considerable role in the self-noise radiation that is hitherto less recognised. When the same trailing edge flat plate is cut into a sawtooth serration shape, the self-noise reduction will be underpinned simultaneously by both the serration effect (dominant) and the blade-loading effect. The results demonstrate that the far-field radiation of a serrated aerofoil can be manipulated significantly depending on the direction of the flap angle. In the flap-down configuration, the blade-loading will become a negative factor that causes a deterioration of the noise reduction performance across the entire frequency range. In the flap-up configuration, three spectral frequencies zones can be defined. At the low-frequency zone, the diminished cross-flow at the sawtooth gaps will impede the noise reduction capability. At the central-frequency zone, the re-distribution of the turbulence sources and reduction in the turbulence spanwise length scales will enhance the noise reduction performance. Improvement in the noise performance can also be achieved at the high-frequency zone owing to the lack of interaction between the cross-flow and sawtooth structure. A new concept is positively demonstrated by varying the serration flap angle as a periodic function across the spanwise direction (spanwise wavy serration). When compared to a non-flap serrated trailing edge, the spanwise wavy serration is found to further increase the noise reduction level between the central and high-frequency regions.

✉ P. C. Woodhead
philip.woodhead@brunel.ac.uk

T. P. Chong
t.p.chong@brunel.ac.uk

P. F. Joseph
pfj@soton.ac.uk

A. Vathylakis
alex.vat@hotmail.com

[1] Department of Mechanical and Aerospace Engineering, Brunel University London, Uxbridge UB8 3PH, United Kingdom

[2] Institute of Sound and Vibration Research, University of Southampton, Southampton SO17 1BJ, United Kingdom

Published online: 05 July 2021

Graphic abstract

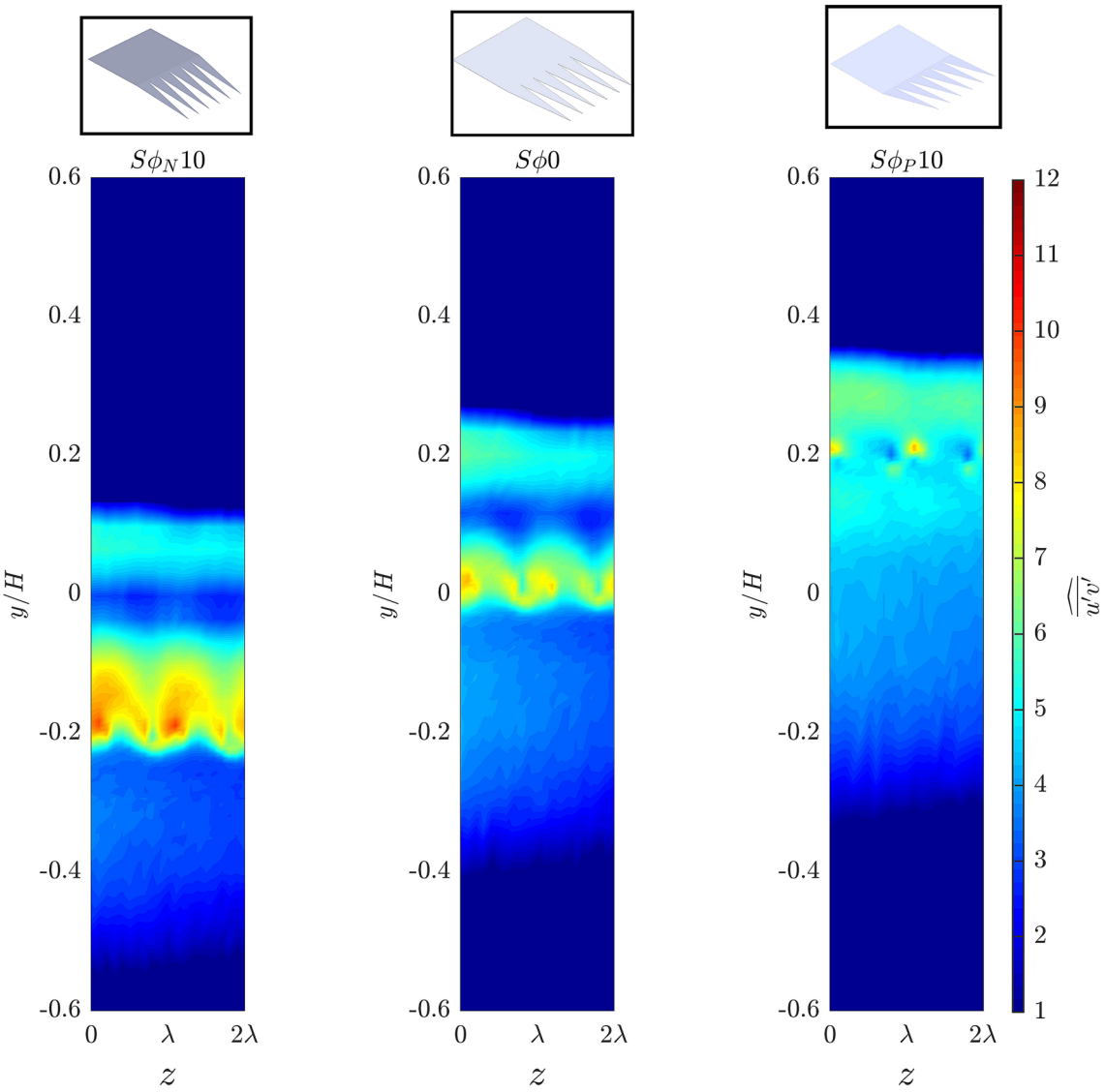

1 Introduction

Self-noise emitted from the trailing edge of an aerofoil blade represents a major environmental and operational issue in the aviation, wind turbine and home appliance industries. There have been continuous efforts in the research community to develop new flow control methods to improve the level of reduction for the trailing edge self-noise. For example, Liu et al. (2019) employ trailing edge flap on their aerofoil to mitigate the stall noise. One of the most commonly used methods to reduce the turbulent boundary layer trailing edge noise of aerofoil is inspired by the owl's wing. The unique feature of trailing edge sawtooth serrations has been successfully demonstrated in wind tunnel experiments with broadband noise reduction typically up to 8 dB (Gruber et al. 2011). Also, reduction in trailing edge noise has been witnessed through the addition of serrations on a real size wind turbine blade by Oerlemans et al. (2009) and Hurault et al. (2015). Although noise reductions were found to be lower than that obtained under laboratory conditions, they still observe overall sound power level reductions on the wind turbine blade up to about 3 dB.

In the early 2010s, Gruber et al. (2011) and Moreau and Doolan (2013) investigate experimentally the influence of different parameters on the noise reduction performance of

flat plate serrations inserted into a cambered aerofoil and flat plate, respectively. After a comprehensive experimental study on many sawtooth geometries, Gruber et al. (2011) establish that significant noise reduction can be achieved if two conditions are fulfilled. As depicted in Fig. 1 for a conventional serration geometry $S\phi0$, the first is when the serration length H is of the same order as the turbulent boundary layer thickness near the trailing edge. The second is when the serration half angle Ψ (also the serration wavelength λ) is small, giving the appearance of a sharp sawtooth. These conditions generally agree well with the recommendation given by Howe (1991). The same observation for the serration length and serration wavelength is also reported by Chong et al. (2013), who investigate several non-flat plate type serrated trailing edges.

Gruber et al. (2011), Chong and Vathylakis (2015) and Avallone et al. (2016) employ various experimental techniques to visualise the three-dimensional flow in the vicinity of the trailing edge serrations. Gruber et al. (2011) employ smoke visualisation technique at the vicinity of their serrated trailing edge, where prominent cross-jet is observed across the sawtooth gaps. They suggest that the interaction between the cross-jet and the sawtooth geometry could cause a noise increase at high-frequency. The cross-jet across the sawtooth gaps is also inferred by Chong and Vathylakis (2015) as a source to trigger the vortical structures at the vicinity of the sawtooth oblique edge to interact with the local turbulent boundary layer. Such viscous and inviscid interaction will re-distribute the momentum and turbulent shear stresses along the sawtooth edges and tips and reduce the acoustical scattering efficiency of the hydrodynamic pressure fluctuation into noise. The phenomenon of flow mixing between the turbulent boundary layer and pressure-driven vortical structure (Chong and Vathylakis 2015) is also evidenced by Jones and Sandberg (2012), Moreau et al. (2016) and Avallone et al. (2016). Employing the volumetric particle image velocimetry technique, Avallone et al. (2016) demonstrate pairs of counter-rotating streamwise-oriented vortical structures in the space between the serrations, which are driven by the mean pressure difference between the suction and the pressure sides of the aerofoil. These structures cause a funnelling effect that acts to distort the mean flow that causes a local variation in the effective angle seen by the turbulent flow approaching the serration edges, resulting in higher surface pressure fluctuations at the root compared with the tip.

The noise performance of a serrated trailing edge can also be influenced by a third sawtooth geometrical variable, which has hitherto received little attention. This geometrical variable is the flap angle (ϕ), or inclination angle relative to the aerofoil camber line of the serrated flat plate, as illustrated in Fig. 1 on a NACA 65(12)–10 aerofoil. When the serration flat plate or element of the sawtooth is deflected "upward" with relative to the zero flap angle, a positive flap angle ϕ_P is produced. Likewise, a "downward" deflection of the serration flat plate will produce a negative ϕ_N. This sign convention is adopted throughout the paper here. As will be shown later, varying the flap angle of the serrated flat plate can produce considerably different noise performances. This has considerable ramification for industrial blades, such as the wind turbine. This is because wind turbine blades that adopt the serration technology can be very susceptible to the misalignment between the incoming flow angle and the serration flap angle.

The change in noise characteristics by serrated trailing edge with flap angle could be attributed to two possible mechanisms. The first is related to the change in *global* flow field around the aerofoil when introducing a flap angle to the serrated flat plate. The different blade-loading will almost certainly affect the growth of boundary layers, thereby resulting in different trailing edge self-noise characteristics. Oerlemans et al. (2009) and Dassen et al. (1996) suggest that flap angle at the serrated trailing edges is the cause for the increase in high-frequency noise, as the serrations are misaligned with the flow in the wake of the aerofoil. The second mechanism is considered as more *localised*. As discussed earlier, serration sawtooth without flap angle can already create a substantial level of three-dimensional flow at the trailing edge to reduce the noise scattering efficiency. It is anticipated that introducing a flap angle to the serrated flat plate will enhance the three-dimensionality of the flow fields at region close to the trailing edge, thereby further affecting the self-noise radiations.

Acre León et al. (2016) study a combined effect of aerofoil angles of attack and serration flap angles (flap-down

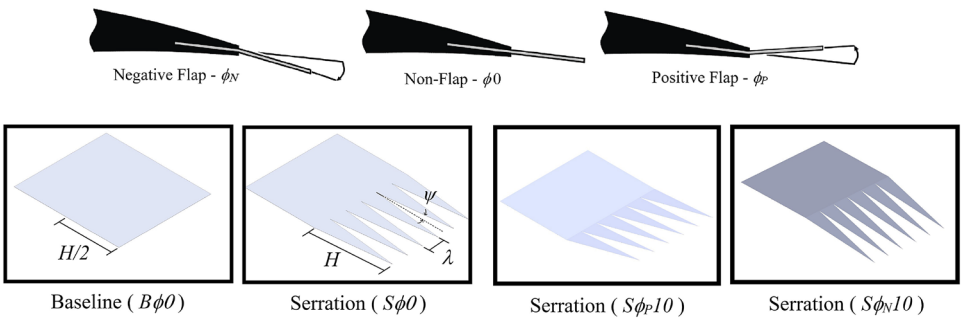

Fig. 1 Geometric parameters of the baseline and serrated trailing edge flat plates for the NACA 65(12)-10 cambered aerofoil: serration amplitude (H), serration wavelength (λ) and flap angle (ϕ). The figure contains some examples of the serration with positive flap angle ($S\phi_P10$) and negative flap angle ($S\phi_N10$)

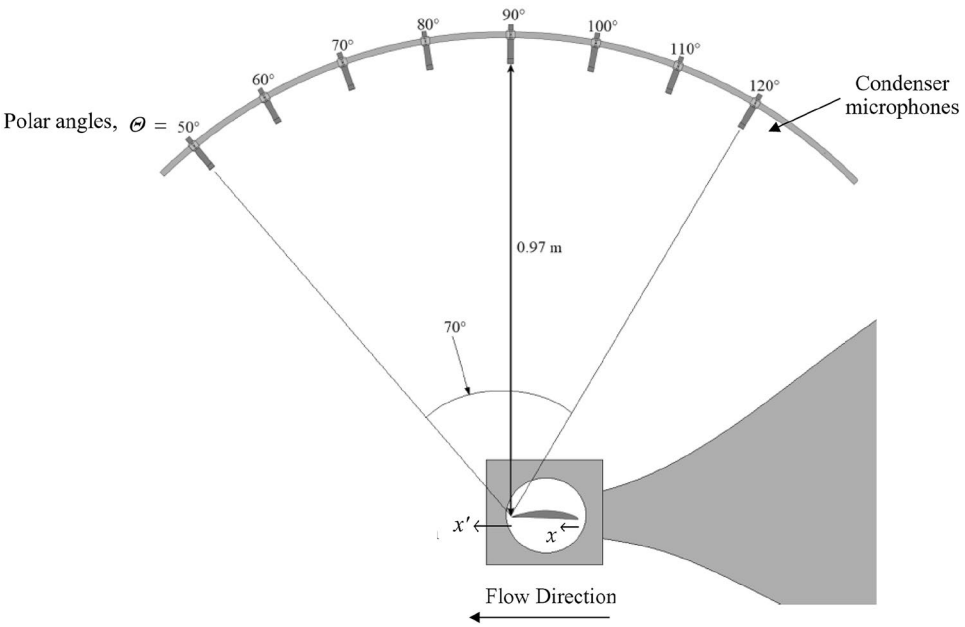

Fig. 2 Schematic of the wind tunnel configuration

only, towards the pressure surface) on a NACA 0018 aerofoil. They observe that the aeroacoustics performance of a serrated trailing edge is more sensitive to the flap angle, rather than the aerofoil incidence angle. Across all the angles of attack investigated, the flap-down serration is found to degrade the noise performance, and in some cases, significant noise increase can be observed at the high-frequency region. Various results presented in the paper on the boundary layer and near wake development all converge to the fact that a flap-down serration can increase the statistical turbulence level in the near field and promote the edge-oriented streamwise vortices. The combination of these effects can impede the aeroacoustics performance of a serrated trailing edge. However, the effect of flap-up for a serrated trailing edge has not been studied in that paper. This gap is partially addressed by Vathylakis et al. (2016) when a flap-up serrated trailing edge is also studied. Albeit using an asymmetrical aerofoil, they also observe the same aeroacoustics trend in the flap-down configuration, but crucially, a mild flap-up serration can actually produce a better noise reduction performance at the central frequency region by a further 2 dB, although a slight degradation in the noise performance at low-frequency is also noted.

The flap angle of a serrated flat plate trailing edge, despite being largely overlooked so far, can certainly represent the 3^{rd} optimisation parameter in addition to the serration amplitude and wavelength to control the aeroacoustics responses. For example, Woodhead et al. (2017) exploit this property to design their serrations with the flap angle as a periodic function in the spanwise direction. They found that a more rapid spanwise waviness of the serration can outperform the noise reduction performance at the central to high-frequency ranges, while remain the same level at the low-frequency, when compared to the non-flap serration. The paper published by Acre León et al. (2016) contains important time-averaged flow quantities in conjunction with the far-field acoustics in third-octave bandwidth. However, there are still some gaps in the literature for a complete understanding of the physical mechanisms, especially the lack of detailed power spectral density and coherence studies between the hydrodynamic and acoustic fields for a serrated aerofoil subjected to nonzero flap angle. An improved understanding of the underlying physics would almost certainly provide a new avenue to elevate the serration technology to the next level. For example, the flexible serrated trailing edge studied by Zhou et al. (2020) is found to achieve additional $2-3$ dB broadband noise reduction at high-frequency. Setting a spanwise periodicity for the trailing edge serrations can also achieve further level of broadband noise reduction (Woodhead et al. 2017). The main objective of this paper, therefore, is to perform an experimental study to investigate the overall performance of serrated and non-serrated trailing edges with different flap angles, and their effects on the far-field radiation, boundary layer near the trailing edge and the near wake velocity generated under a flow condition that comprises a medium level of Reynolds number and a low angle of attack. Note that this paper does not provide a complete parametric study of the effects of serration geometries (amplitude, wavelength and flap angle) across wide ranges of Reynolds number and angle of attack.

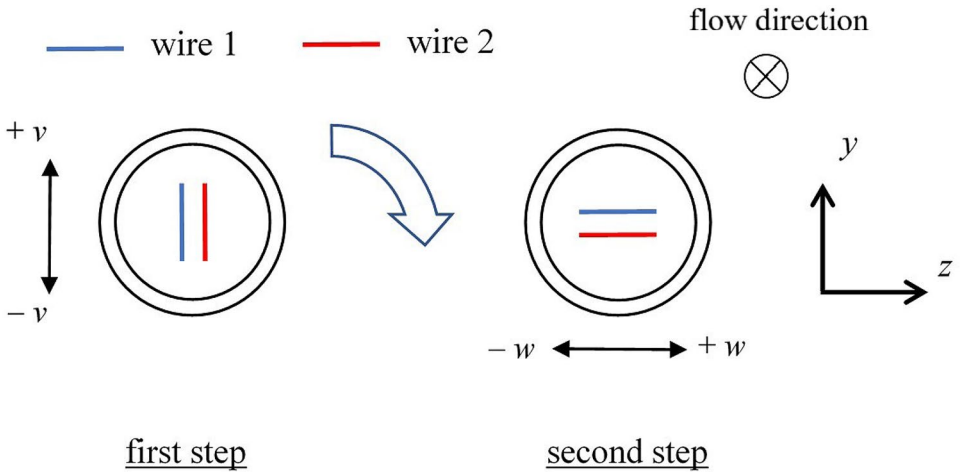

Fig. 3 Schematic describing the two-step approach to measure the v and w velocity components. The main flow direction is pointing towards the plot. Drawings are not to scale

2 Experimental set-up

2.1 Design of the experimental aerofoil and flat plate add-on

The aerofoil model used in this study is the NACA 65(12)-10. This type is commonly adopted in the outlet guided vanes of aircraft engine, or in a compressor cascade. The overall width of the aerofoil is 0.45 m, although only 0.3 m is submerged in the open jet with the excess parts extending beyond the side plates of the open jet nozzle. The nominal chord length of the aerofoil is 0.15 m, but the overall chord length C depends on the type of flat plate trailing edge add-on. In order to achieve the same wetted surface area, the length of the baseline flat plate is always designed to be half of the corresponding serrated flat plate (see Fig. 1). For example, a serrated flat plate of 35 mm in length (i.e. $C = 0.185$ m) will be compared against the baseline flat plate of 17.5 mm (i.e. $C = 0.1675$ m). The flat plate trailing edges are 3D-printed with a printing resolution of 100 microns (0.01 mm) for all the cases.

Figure 1 presents some schematics for the serrated trailing edge with the flap-down (negative flap), non-flap and flap-up (positive flap) configurations. The three serration geometrical parameters are the serration amplitude (H), serration wavelength (λ) and flap angle (ϕ). The baseline (non-serrated) trailing edge is designed as (B), and the serrated trailing edge is (S). These acronyms are used throughout the paper, and the readers can refer to Fig. 1 for the relevant schematic illustrations. In order to focus on the effects of H and ϕ to the self-noise radiation, the serration wavelength is kept the same at $\lambda = 3.3$ mm throughout the experiment. The coordinate system adopted in the current work is defined as follows: streamwise (x), vertical (y) and spanwise (z). The corresponding velocity vector is given by the u, v and w, respectively. Note that the coordinate x has its origin at the aerofoil leading edge. A separate streamwise coordinate definition of x' refers to the origin at the sawtooth tip. This difference will be reminded again later in the paper.

Coarse sandpaper strips are applied to both the suction and pressure surfaces of the aerofoil at $x/C = 0.2$ to trip the boundary layers into turbulent. This is to ensure that turbulent noise source can be generated at the trailing edge. The coarse sandpaper has a thickness of 0.95 mm and width of 10 mm.

The main aerofoil body has a 0.8 mm slot at the rear end, which allows a tight insertion of the trailing edge flat plate of the same thickness. The range of flap angles for both the serrated and non-serrated trailing edge flat plates is investigated at $-15° < \phi < 15°$ at intervals of 5°. In what follows, ϕ_P and ϕ_N denote the positive flap angle (flap-up) and negative flap angle (flap-down), respectively.

The above design will introduce a small geometrical step of 0.2 mm on each side of the trailing edge surface. According to Gruber (2012), the far-field noise is only slightly affected (< 0.5 dB) by this minor discontinuity. This means that any changes in the far-field radiation are predominantly due to the various trailing edge treatments. In the current study, the boundary layers are fully turbulent when reaching the trailing edge. The ratio between the geometrical step and boundary layer displacement thickness ($\frac{t}{\delta^*}$) at the suction side and pressure side near the aerofoil's trailing edge is only 0.13 and 0.05, respectively. Therefore, the small geometrical step is not expected to alter the turbulent boundary layer significantly. In addition, no vortex shedding noise is generated, which is consistent with Blake (1986) who states that $\frac{t}{\delta^*} > 0.3$ represents the criterion to produce the bluntness-induced vortex shedding tone noise.

2.2 Wind tunnel facilities and instrumentation

This section describes the wind tunnel facilities and instrumentation set up for the far-field acoustic and near-field flow measurements, which are both performed at

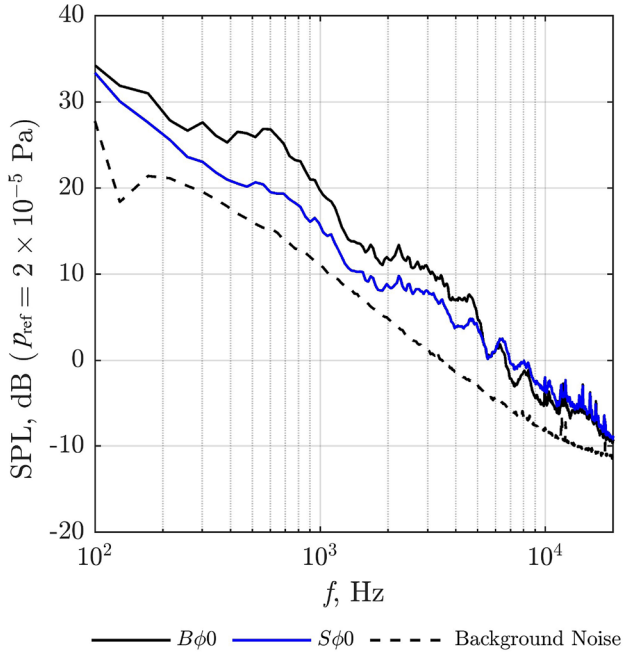

Fig. 4 Comparison of the SPL, dB, produced by the $B\phi0$ ($H = 15$ mm) and $S\phi0$ ($H = 30$ mm, $\lambda = 3.3$ mm) trailing edges at $U_\infty = 24\,\mathrm{ms}^{-1}$ and $\theta = 0°$

the aeroacoustics facility at Brunel University London (see Fig. 2). The open jet wind tunnel is situated inside a 4 m × 5 m × 3.4 m anechoic chamber. The nozzle exit is rectangular with dimensions of 0.10 m (height) × 0.30 m (width). The jet velocity (U_∞) can reach $80\,\mathrm{ms}^{-1}$, but in the current work the jet velocity is fixed at $U_\infty = 24\,\mathrm{ms}^{-1}$ only, corresponding to a representative Reynolds number of about 2.96×10^5 based on the overall aerofoil chord. The open jet wind tunnel can produce low turbulence intensity of 0.1%–0.2% at $U_\infty \approx 30\,\mathrm{ms}^{-1}$. The background noise (without the presence of the aerofoil, but with the side-plate in place) is largely contributed by the low subsonic jet noise, which is very low in comparison with the aerofoil self-noise level produced at the identical flow speed. All the far-field noise and flow measurements are performed at a geometric angle of attack for the aerofoil at $\theta = 0°$. It is important to emphasise that all the aeroacoustics behaviours and flow physics discussed in this paper, including any references to the acoustic and hydrodynamic spectral frequency in dimensional form, are only pertinent to a flow condition that comprises medium level of Reynolds number and low angle of attack.

The far-field noise measurements are performed with eight 1/2-inch condenser microphones (G.R.A.S. 46AE). As shown in Fig. 2, the microphones are positioned at equal distance to the trailing edge of 0.97 m at the mid-span across a range of polar angles $50^o \le \Theta \le 120^o$, with 10^o interval. The acoustic data are acquired using a 16-bit analogue-digital card manufactured by the National Instrument. The sampling frequency is 40 kHz with a sampling time of 20 seconds. The sampled data are then windowed, and the power spectral density (PSD) of 1 Hz bandwidth is computed from a 1024-point Fast Fourier Transform (FFT) with a frequency resolution of 39 Hz and a 50% overlap time.

The sound pressure level is denoted as SPL and given by the following equation:

$$\mathrm{SPL}(f) = 20 \log_{10} \left[\frac{p(f)}{p_{\mathrm{ref}}} \right], \ \mathrm{dB} \tag{1}$$

where p is the root mean square of the acoustic pressure and $p_{\mathrm{ref}} = 20\,\mu\mathrm{Pa}$ is the reference pressure.

The sound power level, PWL, can be calculated based on an assumption that the acoustic waves from the aerofoil trailing edge are radiated in a cylindrical fashion. The PWL radiated per unit span in the range of polar angles between $50^o(\Theta_1) \le \Theta \le 120^o(\Theta_8)$ is calculated by the following equations:

$$\mathcal{W}(f) = \frac{2\pi \int S_{pp}(f, \Theta) \Delta\Theta}{\rho c_\infty} \tag{2}$$

$$\mathrm{PWL}(f) = 10 \log_{10} \left[\frac{\mathcal{W}(f)}{\mathcal{W}_0} \right], \ \mathrm{dB} \tag{3}$$

where S_{pp} is the far-field pressure power spectrum density at a polar angle Θ, where $\Delta\Theta = 10° \times \frac{\pi}{180}$ is the angle between adjacent microphones in radian, and $\mathcal{W}(f)$ is the sound power integrated for the radiation angles from Θ_1 to Θ_8, with intervals of 10°, $\mathcal{W}_0 = 10^{-12}$ W, $c_\infty = 343\,\mathrm{ms}^{-1}$ is the speed of sound for air and $\rho = 1.225\,\mathrm{kgm}^{-3}$ is the air density.

The overall sound power level (OAPWL) of the aerofoil self-noise defined within a frequency range f can be represented by:

$$\mathrm{OAPWL} = 10 \log_{10} \left[\frac{\int_f \mathcal{W}(f) df}{\mathcal{W}_0} \right], \ \mathrm{dB}. \tag{4}$$

To investigate the upstream boundary layer profile of the baseline and serrated trailing edges, a single hot-wire probe (5 μm diameter, 1.25 mm length, DANTEC 55P11) is used to measure the mean and fluctuating velocities. The hot-wire is operated at an overheat ratio of about 1.8, which achieves a good velocity sensitivity in the measurements. To determine the location of the hot wire probe with respect to the aerofoil surface, a very lightweight metal shim of a pre-determined thickness is placed on the surface before the experiment. The hot wire probe is then traversed with an incremental step of 0.05 mm towards the metal shim. As soon as the first contact between the hot wire prongs with the metal shim surface is made (monitored by a multi-meter),

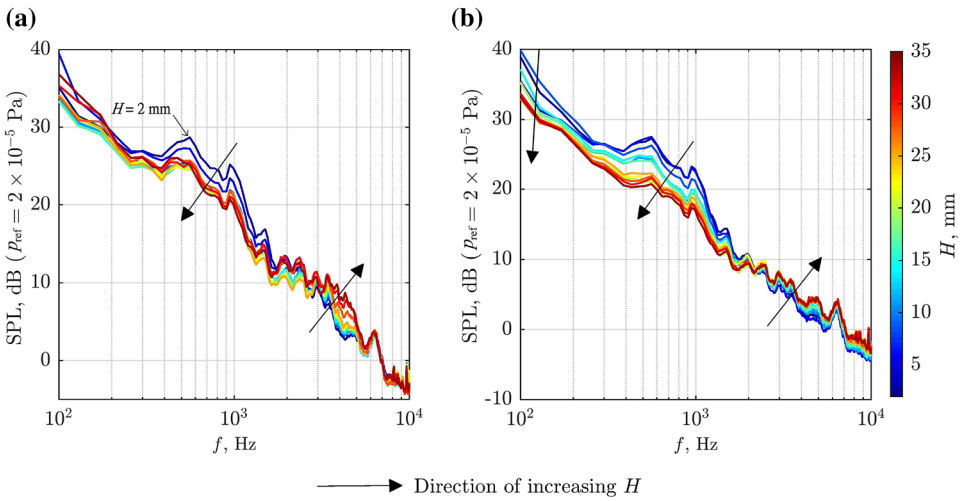

Fig. 5 Comparison of the SPL, dB, produced by the **a** $B\phi0$ baseline trailing edges, and **b** $S\phi0$ serrated trailing edges ($\lambda = 3.3$ mm), both as a function of the H (2 mm $< H <$ 35 mm), at $U_\infty = 24\,\mathrm{ms}^{-1}$ and $\theta = 0°$

we can estimate that the hot wire probe is now at a height equivalent to the thickness of the metal shim with respect to the aerofoil surface.

The near wake velocity power spectral densities and coherence function in the spanwise direction are also investigated by two single hot-wire probes—one is termed as a "stationary probe" and another one is called the "traversing probe". The overheat ratio in this case is adjusted to a slightly lower value of 1.6 for both hot-wire probes. This is to minimise the thermal interference when the two probes are in close proximity to each other during the coherence measurement. An X-wire probe (5 μm diameter, 1.25 mm length, DANTEC 55P61) is used to measure two velocity components simultaneously in the near-wake flow field. Measurements are taken across selected two-dimensional y-z and x'-y planes, set up in reference to the coordinate system indicated in Fig. 9a. For each measurement point, the three velocity components (u, v, and w) are acquired in a two-step approach. In the first step, the probe is positioned as shown in Fig. 3. This configuration corresponds to the velocity acquisition of the u and v. When all the pre-set grid points have been measured using the configuration depicted in the first step, the probe will then be rotated by 90° about its stem, whose configuration is now depicted as the second step in Fig. 3. After that, the probe will move back to the first grid point, and then, another velocity acquisition will commence again for the same grid points. This time, it will facilitate the velocity acquisition of the u and w. During the experiment, the overheat ratio for both wires is set at 1.6, a value that is a compromise between achieving an acceptable velocity sensitivity and minimal thermal interference between the wires at low speed. Both the effective cooling velocity calibration and yaw calibration of the X-wire are carried out *in situ*. Once the yaw factors are determined, they will be applied alongside the effective cooling velocities measured by wire 1 and wire 2, respectively, to calculate the velocity components u, v (first step) and u, w (second step). Readers can refer to Garcia Sagrado (2008) for detailed explanation of the procedures and relevant mathematical derivations. Temperature correction to the acquired voltages for both the single and X-wire is applied throughout the measurement campaign.

Signals from both the single and X-wire probes are digitised by a 12-bit A/D converter (TSI model ADCPCI) at a sampling frequency of 20 kHz for 120000 realisations. The hot-wire probes are attached to a computer-controlled three-dimensional traverse system with a resolution of 0.01 mm in all the axes. More details about their operating procedure are discussed in Sect. 3.2.

3 Results

Discussion in this section will focus on both the far-field spectral characteristics (Section 3.1) and the near-field statistical properties (Section 3.2) pertaining to the baseline and serrated aerofoils. The analysis will be based on the aeroacoustics performance of the flat plate trailing edges with and without flap angle ϕ. As mentioned earlier, the wind tunnel velocity is set at $U_\infty = 24\,\mathrm{ms}^{-1}$ and angle of attack $\theta = 0°$ for all the cases considered here.

3.1 Far-field spectral characteristics

3.1.1 Trailing edge flat plate with zero flap angle $\phi = 0°$

This sub-section will focus only on the aerofoil self-noise radiation at $\phi = 0°$. It will begin with some presentations of the SPL of the baseline and serrated aerofoil. The narration will then shift to the quantification of noise reduction/increase by the serrated trailing edge with amplitude H, which is measured against the baseline (straight, non-serrated) trailing edge of $H/2$. This approach is illustrated in Fig. 1 and has been adopted by Gruber (2012) and many others to ensure the same wetted area for both the serrated

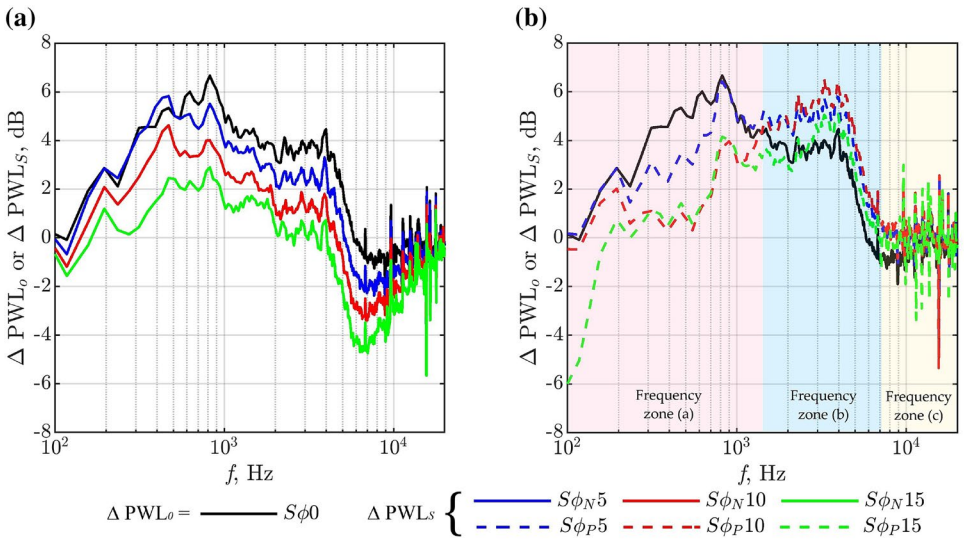

Fig. 6 Comparison of the ΔPWL$_S$, dB, produced by **a** $S\phi_N5$, $S\phi_N10$ and $S\phi_N15$, and **b** $S\phi_P5$, $S\phi_P10$ and $S\phi_P15$, where $H = 30$ mm, $\lambda = 3.3$ mm, under $U_\infty = 24\,\text{ms}^{-1}$ and $\theta = 0°$. Note that the ΔPWL$_o$ produced by the $S\phi0$ is also included for both the sub-figures

and baseline aerofoils. This definition is adopted throughout this paper.

Figure 4 shows an example of the acoustic spectra containing self-noise radiation by the baseline and serrated aerofoils, including the background noise of the open jet wind tunnel. Similar to the study by Vathylakis et al. (2016), who used the same facility, the background noise from the open jet flow (i.e. without the aerofoil, but with the presence of the side holding plates) is shown to be significantly lower than the self-noise produced by the quietest serrated aerofoil across the entire frequency range of interest. The SPL spectrum produced by the serrated aerofoil is lower than that produced by the baseline aerofoil over a significant portion of the low-to-central frequency region. However, noise increase can also be observed at $f > 6$ kHz. The same characteristics are also reported in the previous studies (Oerlemans et al. 2009; Dassen et al. 1996; Acre León et al. 2016; Vathylakis et al. 2016; Gruber 2012) for a non-flap ($S\phi0$-type) serrated aerofoil. After analysing many dataset in the context of non-dimensional frequency, $f\delta/U_\infty \approx 1$ is found to be the condition for a serrated aerofoil to switch from a positive performance of broadband noise reduction to a negative outlook with higher noise level than the baseline aerofoil (Gruber 2012). Here f is the frequency, and δ is the turbulent boundary layer thickness near the trailing edge. It has been established that the reduction in broadband noise at the low-to-central frequency is attributed to the serration effect. The noise increase at the high-frequency, however, is proposed by Gruber (2012) to be the byproduct of the interaction between the cross-flow and the sawtooth edges.

Here, the effect of the trailing edge flat plate length for the self-noise radiation is investigated for both the baseline $B\phi0$ and serrated $S\phi0$ aerofoils between $2 \le H \le 35$ mm. Figure 5a shows the noise spectra for the baseline $B\phi0$ trailing edge at $U_\infty = 24\,\text{ms}^{-1}$, $\theta = 0°$ and $\phi = 0°$. It is reasonable to treat the $H = 2$ mm as the closest configuration to the unmodified NACA 65(12)-10 shape. By simply increasing the H against the above reference, broadband noise reduction can already be realised between $0.25 \le f \le 2.5$ kHz. The level of noise reduction is also found to improve as H increases. However, at $2.5 \le f \le 5$ kHz, the radiated noise level increases as the H increases. It is important to state that the noise increase observed here is not contributed by the cross-flow because the flat plates for the $B\phi0$ do not feature any air gaps.

In general, increasing H will cause a reduction in noise level at low-frequency, but increase in noise level at high-frequency. This trend suggests that the self-noise radiation is a function of the boundary layer properties near the flat plate trailing edge. However, as one would expect the turbulent boundary layer near the trailing edge to become thicker when H increases, the increase in size of the largest eddy scale in the boundary layer would normally translate into increase in noise level at low-frequency, and reduction in high-frequency noise levels. This reasoning, however, contradicts the measured noise spectra in Fig. 5a. This implies that the change in noise characteristics as a function of H is more related to the change in the blade-loading. The resulting shift in the leading edge stagnation point as H varies could cause an inhomogeneous development of the boundary layers at the suction and pressure surfaces. It is possible that the cumulative eddy size between the suction and pressure surfaces at the vicinity of the trailing edge is actually smaller as H increases. Further investigation is certainly needed to verify this conjecture.

Figure 5b shows the noise spectra for the $S\phi0$ trailing edges at the same geometrical and flow conditions. For consistency, the serration wavelength, $\lambda = 3.3$ mm is maintained for all the serrated cases. The serrated trailing edges also exhibit a similar trend as the baseline trailing edge

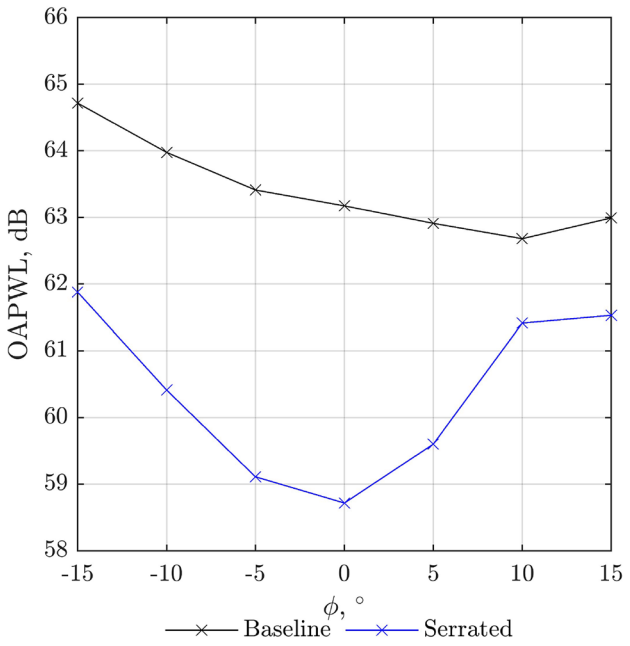

Fig. 7 Comparison of the OAPWL, dB, integrated between $0.2 \leq f \leq 7$ kHz of the baseline and serrated trailing edges as a function of the flap angles (ϕ) at $U_\infty = 24\,\mathrm{ms}^{-1}$ and $\theta = 0°$

discussed earlier. For a slightly different frequency range of $0.1 < f < 2.5$ kHz, the quietest serration configuration is associated with the largest H. It is interesting to note that, at 100 Hz, increasing the H of the serrated flat plate can reduce the noise in a consistent manner. This implies that the serrated flat plate has a considerable effect on the blade-loading. Generally, the $S\phi 0$ is considerably more effective than the $B\phi 0$ to accomplish noise reduction as a function of H. The radiated noise level is also found to increase as a function of H at high-frequency for the serration. However, the frequency that marks the onset of noise increase is almost constant at $f \approx 2.5$ kHz for the $S\phi 0$ for the entire range of H considered here. Therefore, the high-frequency noise source is unlikely to be governed by the boundary layer properties at the trailing edge as it does not exhibit the Strouhal number effect.

The results presented in Fig. 5 demonstrate that both the $B\phi 0$ and $S\phi 0$ can manipulate the self-noise radiation as a function of H in a similar fashion, albeit with different sensitivity levels. From the comparison made in Vathylakis et al. (2016), the serrated flat plate with a low H is found to be more effective to reduce the high-frequency broadband noise, while a moderately high H is more effective to reduce the low-to-central frequency broadband noise. The exception is when $H \geq 30$ mm for the $S\phi 0$, where it is effective to reduce the broadband noise across the entire low-to-high-frequency range. This particular configuration for the serration ($\lambda = 3.3$ mm, $H = 30$ mm $\longrightarrow \lambda/H = 0.11$), therefore, is chosen for further investigation on the sensitivity of aerofoil self-noise radiation subjected to flap angle. The results will be discussed in the next section.

3.1.2 Trailing edge flat plate with nonzero flap angles, $\boldsymbol{\phi \neq 0°}$

This section will investigate the effect of the aerofoil self-noise radiation subjected to trailing edge flat plates with nonzero flap angles. Using the same definition, the serrated flat plate of $H = 30$ mm will be compared against the baseline straight flat plate of $H = 15$ mm. This applies to all the nonzero flap angle configurations. The naming convention of different trailing edge flat plates will be informed by either the ϕ_P or ϕ_N, which refers to the positive (flap-up) or negative (flap-down) flap angle, respectively (see Fig. 1). For example, a serrated flat plate with $\phi = +10°$ will be denoted as $S\phi_P 10$; a baseline flat plate with $\phi = -5°$ will be denoted as $B\phi_N 5$ and so on. This naming strategy will be adopted throughout the rest of the paper.

To quantify the effect of flap angles to the serrated flat plates (as well as the straight, non-serrated flat plates), one can examine the $\Delta\mathrm{PWL}_i$, which is defined as the difference in the sound power level, as a function of frequency, in the following:

$$\Delta\mathrm{PWL}_i(f) = \mathrm{PWL}_{B\phi 0}(f) - \mathrm{PWL}_j(f)$$
$$i = \begin{cases} B, & \text{if } j = B\phi_P \text{ or } B\phi_N \\ S, & \text{if } j = S\phi_P \text{ or } S\phi_N \\ o, & \text{if } j = S\phi 0 \end{cases} \tag{5}$$

Essentially, Equation (5) stipulates that the reference aerofoil, whose sound power level radiation represents the fundamental value, is the $B\phi 0$. Therefore, when the subscript i in Equation (5) is B, the comparison is between the $B\phi 0$ and the straight, non-serrated flat plate trailing edge with either a negative or positive flap angle. When the subscript i is S, the comparison is between the $B\phi 0$ and a serrated flat plate trailing edge with either a negative or positive flap angle. Finally, if the subscript i is o, the comparison does not consider the flap angle effect for the serrated flat plate, which would conform to the default comparison as commonly defined in the literature. It should be noted that a positive value of $\Delta\mathrm{PWL}_i$ represents noise reduction, and the opposite is true for a negative $\Delta\mathrm{PWL}_i$.

The $\Delta\mathrm{PWL}_S$ at various flap angles are demonstrated in Figure 6. The results follow largely the same trends as observed previously by Vathylakis et al. (2016). Figure 6a compares the $\Delta\mathrm{PWL}_S$ spectra for all the negative flap angles, ($S\phi_N 5$, $S\phi_N 10$, $S\phi_N 15$), including the $\Delta\mathrm{PWL}_o$ by the $S\phi 0$ serrated trailing edge to serve as the reference. The $S\phi 0$ is shown to achieve broadband noise reduction across a wide

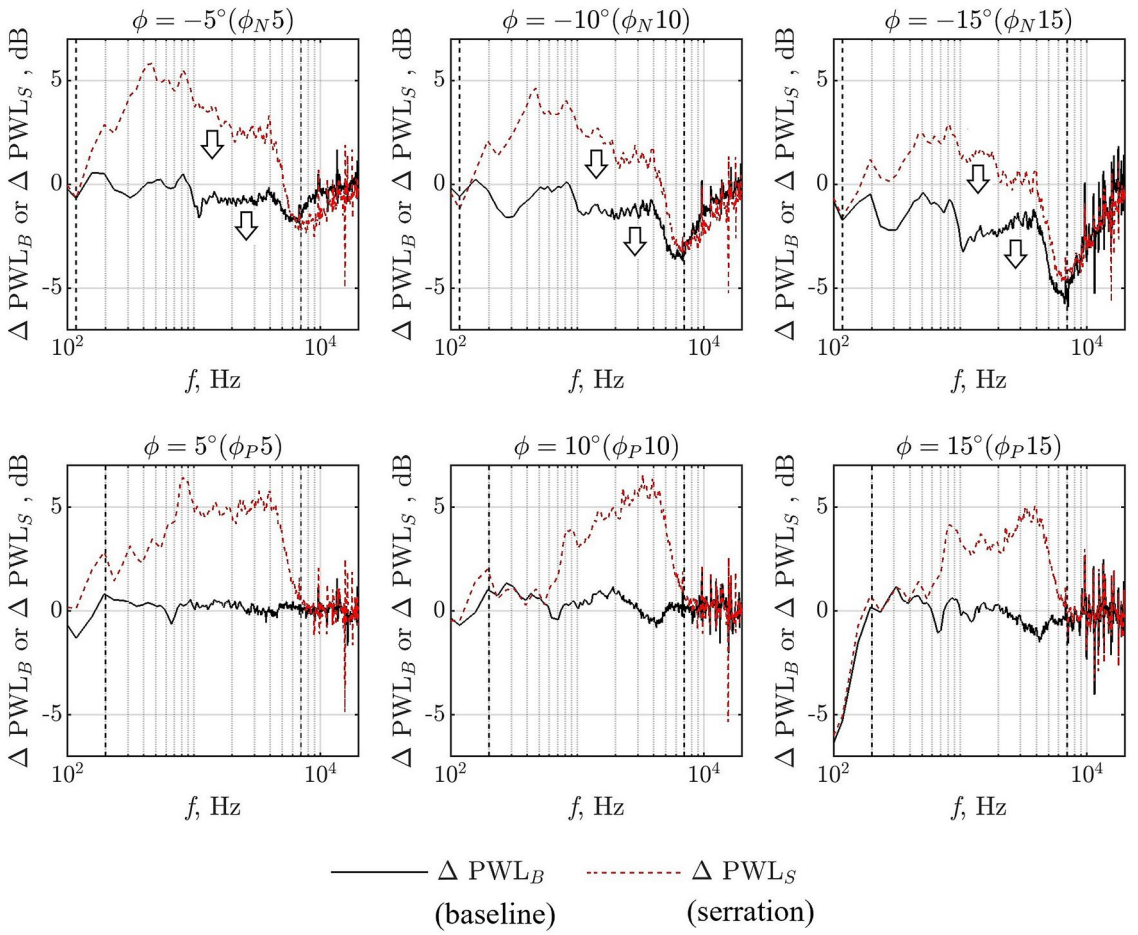

Fig. 8 Comparison between the ΔPWL$_B$ and ΔPWL$_S$, dB, for the baseline and serrated trailing edges, respectively, across $-15° \le \phi \le 15°$, at $U_\infty = 24\,\mathrm{ms}^{-1}$ and $\theta = 0°$

range of frequency up to $f \approx 6$ kHz. Beyond this frequency, noise increase is observed. This is consistent with the SPL spectrum shown in Fig. 4. Interestingly, deflecting the serration flap angle downward would exclusively return a deterioration of the aeroacoustics performance. Although the spectra shapes of the $S\phi_N 5$, $S\phi_N 10$, $S\phi_N 15$ resemble closely to that produced by the $S\phi 0$, the ΔPWL$_S$ level across almost the entire frequency range will drop further whenever the negative flap angle is increased further. Moreover, a larger flap-down angle of the serration not only can result in higher level of noise increase in the high-frequency region, but it can also cause the onset frequency for the noise increase to happen earlier.

On the other hand, the $S\phi_P$ configurations in Fig. 6b produce a more positive outlook in comparison with the $S\phi_N$ trailing edges. Different spectral characteristics of the ΔPWL$_S$ achieved by the serrated $S\phi_P$ trailing edges are manifested in three unique frequency zones: (a) $0.1 < f < 1.5$ kHz, (b) $1.5 < f < 7$ kHz and (c) $f > 7$ kHz. In frequency zone (a), producing a flap-up angle for the serrated trailing edge will lower the level of ΔPWL$_S$. Although the trend is similar to the $S\phi_N$-typed serrated trailing edges, the $S\phi_P$ is more sensitive to the flap angle at this frequency zone. For the $S\phi_P 10$ and $S\phi_P 15$, the noise difference at some frequencies are hovering at ΔPWL$_S \approx 0$ (i.e. no noise reduction). Nevertheless, all the $S\phi_P$ serrated trailing edges would start to recover in their ΔPWL$_S$ level at increasing frequency. The recovery even surpasses the ΔPWL$_o$ reference level in the frequency zone (b). This means that all the $S\phi_P$ trailing edges can outperform the $S\phi 0$ trailing edge within this frequency zone. For example, the ΔPWL$_S$ at $f = 4.0$ kHz achieved by the $S\phi_P 10$ and the $S\phi 0$ trailing edges are 6.2 dB and 4.2 dB, respectively. This represents a 2 dB further level of noise reduction. Finally, the ΔPWL$_S$ produced by all the $S\phi_P$ serrated trailing edges remain positive at the frequency zone (c), i.e. noise reduction continues to occur. This is in contrast with

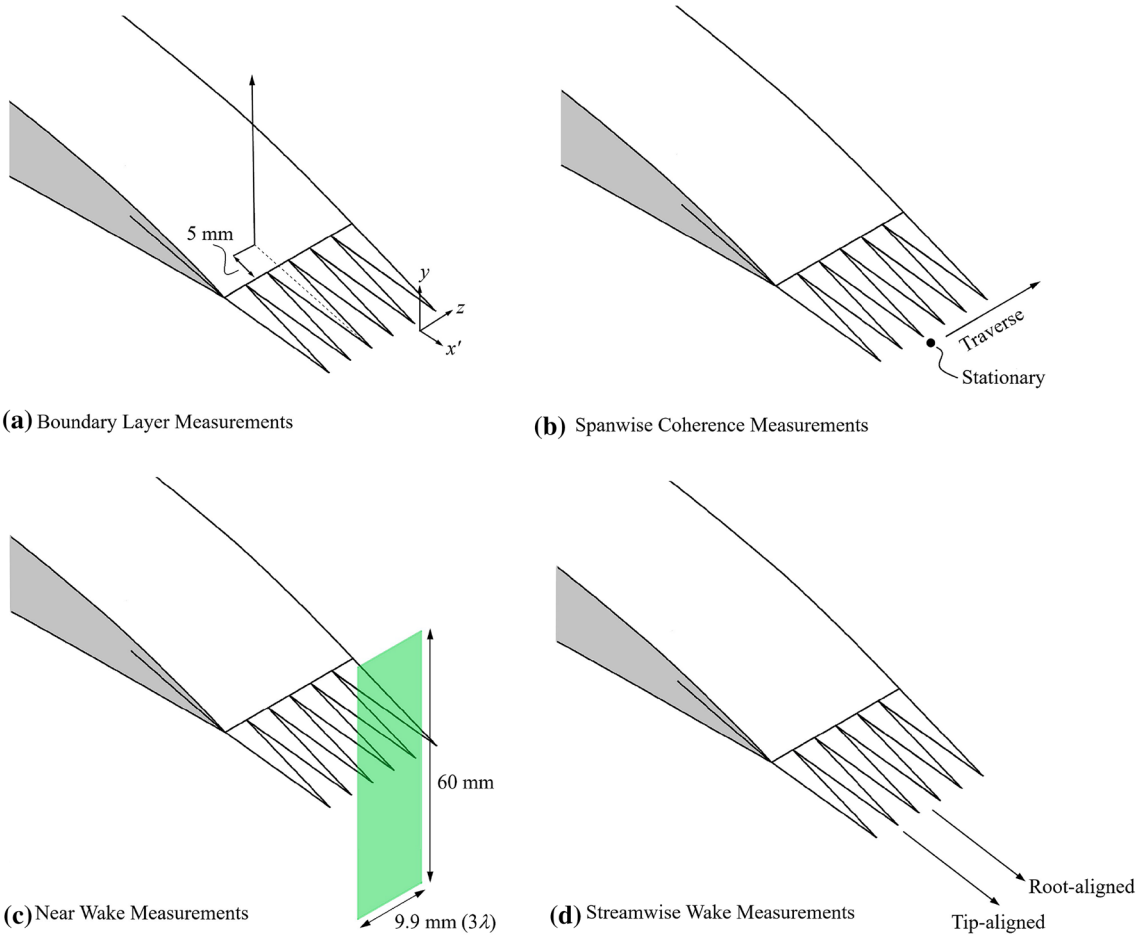

Fig. 9 Schematics illustrating the locations and coverage for the **a** boundary layer measurements, **b** spanwise coherence measurements, **c** near wake measurements and **d** streamwise wake measurements

the $S\phi 0$ serrated trailing edge which is characterised by noise increase throughout the frequency zone (c).

Figure 7 presents the variation in the overall sound power level, OAPWL, integrated between $0.2 \leq f \leq 7$ kHz for the baseline and serrated trailing edges across $-15° \leq \phi \leq 15°$. Initially peaked at $\phi = -15°$ (i.e. $B\phi_N 15$), the results of the baseline trailing edge show a continuous drop of the OAPWL as a function of ϕ towards the positive (flap-up) up to $B\phi_P 10$, before slightly picking up the OAPWL again at $B\phi_P 15$. For the serrated trailing edge, the results show a significant reduction in the OAPWL against the baseline for all the flap angles tested here. An interesting aspect of the serrated trailing edge subjected to the misalignment is the presence of an almost parabolic curve mirrored at the $\phi = 0°$ vertical axis line. This means that, as far as the overall sound performance is concerned, to achieve the quietest serration configuration one has to avoid any serration flap angle. However, the spectral characteristics of the radiated far-field noise by the individual flap-alignment configuration are more complex, as demonstrated in Fig. 6. The underlying mechanisms that cause the behaviours in Fig. 6a for the $S\phi_N$, as well as different spectral characteristics of the three frequency zones for the $S\phi_P$ in Fig. 6b, cannot be answered by the acoustic results alone. In the next section, analysis of the boundary layer and near-wake will be performed to shed some lights of the manipulated flow dynamics by the misaligned serrated trailing edges and their effect on the radiated noise spectral characteristics.

3.2 Investigation of the noise mechanisms

3.2.1 Blade-loading effect and serration effect on the self-noise radiation

In the previous section, the quantification of the noise increase or reduction is measured against the reference baseline $B\phi 0$, as defined in Equation (5). When a baseline

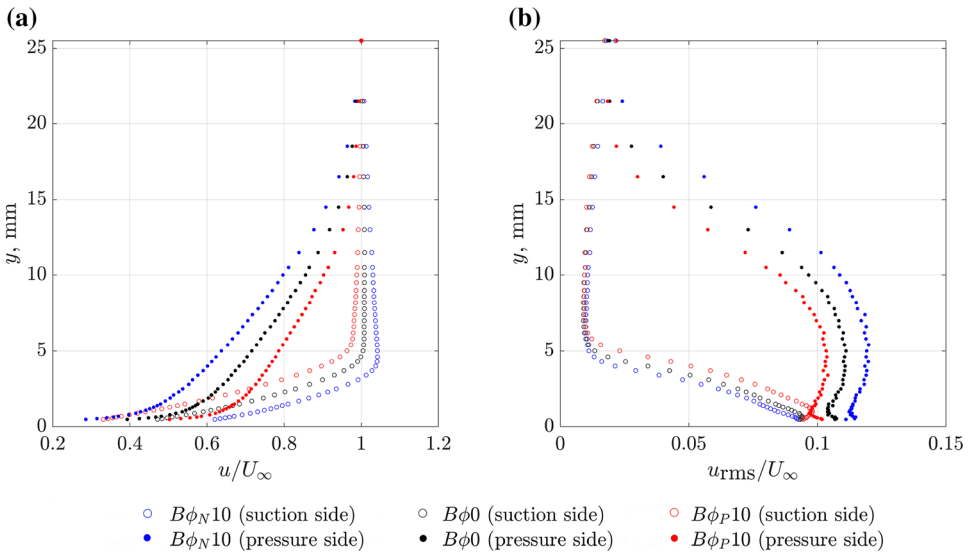

Fig. 10 Comparisons of the boundary layer **a** mean velocity profiles and **b** turbulence intensity profiles, subjected to different flap angles for the baseline trailing edge flat plates ($B\phi_N10$, $B\phi0$ and $B\phi_P10$) at $U_\infty = 24\,\mathrm{ms}^{-1}$ and $\theta = 0°$. The comparison contains the mean and turbulence velocity profiles measured at the suction and pressure surface, all taken at $x = 145$ mm

straight trailing edge is subjected to a nonzero flap angle, the configuration is analogous to an aircraft wing or tailplane deployed with flap setting at the rear. This kind of manoeuvre is known to alter the entire pressure loading of the wing or tailplane, thus changing the lift coefficients. The growth of boundary layers could be very sensitive to the pressure loading of an aerofoil, which can in turn affect the level and spectral characteristics of the radiated self-noise. Indeed, it will be shown later that the $\Delta\mathrm{PWL}_B$, as a function of frequency, is nonzero for some cases. Therefore, it is necessary to make a distinction when a change in the noise level occurs as a direct result of the changes in the pressure loading. This type of noise manipulation by the flap angle is also related to the "blade-loading effect". Note that it is different from the "serration effect" when noise reduction/increase occurs as a result of the serrated trailing edge.

The key question is whether or how much the blade-loading effect contributes to the $\Delta\mathrm{PWL}_S$ in Fig. 6 by the serrated trailing edges. To provide some hints, Fig. 8 shows the comparison between the $\Delta\mathrm{PWL}_B$ and $\Delta\mathrm{PWL}_S$ at their respective flap angles. For the negative flap angles $\phi_N = -5°, -10°$ and $-15°$, noise reduction can generally be observed at low-to-central frequencies for the $\Delta\mathrm{PWL}_S$ by the serrated trailing edges. It is also obvious that the absolute level of $\Delta\mathrm{PWL}_S$ drops as the ϕ_N becomes more negative (larger flap-down angle). This phenomenon follows the trend exhibited by the straight flat plates $\Delta\mathrm{PWL}_B$, where the value changes from $\approx 0\,\mathrm{dB}$ at ($\phi_N = -5°$) to $\approx -1.8\,\mathrm{dB}$ at ($\phi_N = -15°$). This indicates that in a flap-down configuration for a serrated trailing edge, the manipulated boundary layers as a result of the blade-loading effect (to be shown later) have a profound detrimental effect on its effectiveness in the reduction of the self-noise. This will lead to two important outcomes: (1) the blade-loading effect co-exists with the serration effect in a flap-down configuration for the serrated trailing edges at $0.1 \leq f \leq 7$ kHz (as indicated by the vertical dashed lines in Fig. 8), and (2) the blade-loading effect counteracts against the serrated trailing edge for its effectiveness in the reduction of the self-noise radiation.

However, at $f > 7$ kHz, the far-field radiation by the serrated trailing edge is only dominated by the blade-loading effect. This is manifested by the collapse of both the predominantly negative values of $\Delta\mathrm{PWL}_B$ and $\Delta\mathrm{PWL}_S$.

The analysis now focuses on the positive flap angles $\phi_P = 5°$, 10° and 15°. The $\Delta\mathrm{PWL}_B$ at $f \geq 200$ Hz produced by the baseline trailing edges remains largely zero across the entire range of positive flap angles investigated here. Clearly, this indicates that the blade-loading effect cannot be a dominant factor for the aeroacoustics radiation in a flap-up configuration. This is reflected by the corresponding $\Delta\mathrm{PWL}_S$ where the spectral variation as a function of the ϕ_P does not exhibit any discernible trend. Rather, the unique spectral characteristic of the $\Delta\mathrm{PWL}_S$ produced by the serrated trailing edge of various flap-up configurations at $0.2 \leq f \leq 7$ kHz is governed by a more localised flow field manipulation, which will be extensively discussed in the next sections. Again, it is important to emphasise that the blade-loading has a minimal effect at ϕ_P.

3.2.2 Flow study of the boundary layer and wake properties

In order to shed some lights on the manipulated hydrodynamic fields of aerofoil subjected to serrated trailing edges with flap angle, and most importantly their effects on the aerofoil self-noise radiation, some boundary layer and wake flow measurements were performed in the same aeroacoustics facility under the same flow setting as the noise tests.

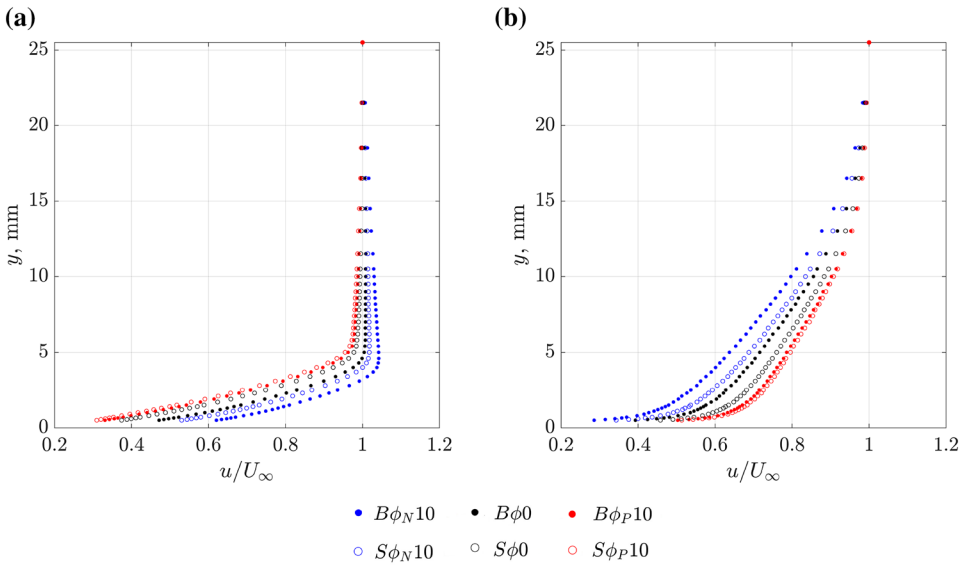

Fig. 11 Comparisons of the boundary layer mean velocity profiles taken at $x = 145$ mm for the **a** suction surface, and **b** pressure surface, subjected to different flap angles for both the baseline and serrated trailing edge flat plates ($B\phi_N10$, $S\phi_N10$, $B\phi0$, $S\phi0$, $B\phi_P10$ and $S\phi_P10$) at $U_\infty = 24\,\mathrm{ms}^{-1}$ and $\theta = 0°$

The schematic of the experimental set-up for the hot-wire measurements is shown in Fig. 9. Note that Fig. 9a contains the coordinate system used in the current study. The streamwise location has two definitions: x' has the origin coincided with the serration tip, whereas the x starts from the aerofoil leading edge (not shown here). The boundary layer measurements are performed on both the suction and pressure surfaces of the aerofoil. The measurement point at each surface is always positioned at the identical location, i.e. 5 mm upstream of the interface between the aerofoil and trailing edge flat plate. For the serrated trailing edge, it would be 5 mm upstream of the interface as demonstrated in the schematic of Fig. 9a. We also ensure that the spanwise location of the boundary layer measurement aligns with the location of one of the sawtooth tips. This particular spanwise location is denoted as z_o. Each boundary layer profile contains 46 points, with a finer spatial resolution at the near wall region achieving $\Delta y \approx 0.05$ mm. The nearest measurement point with relative to the aerofoil surface is about 0.5 mm.

Figure 9b represents the set up for the measurement of the near-wake turbulent velocity by two single hot-wire probes—one is termed as the "stationary" probe and another is called the "traversing" probe. The use of two hot-wire probes is to determine the magnitude squared spanwise coherence of the near-wake turbulent velocity, γ^2, which is defined as:

$$\gamma^2(z,f) = \frac{|\boldsymbol{\Phi}_{v_iv_j}(z_o:z,f)|^2}{\boldsymbol{\Phi}_{v_iv_i}(z_o,f)\,\boldsymbol{\Phi}_{v_jv_j}(z,f)}, \tag{6}$$

where $0 \le \gamma^2 \le 1$. $\boldsymbol{\Phi}_{v_iv_j}(z_o:z,f)$ is the cross-power spectral density between the two streamwise fluctuating velocity signals v_i and v_j. The velocity measurement v_i is measured by the "stationary" probe at $x' = 1$ mm (downstream of the serration tip), $y = 0$, and $z = z_o$. The velocity measurement v_j is measured by the "traversing" probe situated at the same x' and y locations, but traverses along the spanwise z direction. $\boldsymbol{\Phi}_{v_iv_i}(z_o,f)$ and $\boldsymbol{\Phi}_{v_jv_j}(z,f)$ are the auto power spectral density of each individual fluctuating velocity signal. The coherence function provides information about the frequency content of the cross-correlation pertaining to a turbulent structure. A longitudinal coherence can tell us the decay of the eddies, while a spanwise/lateral coherence relates to the physical size of the turbulent eddies.

The X-wire flow measurements produce a series of two-dimensional wake profiles in the y–z plane at $x' = 1$ mm downstream of the tip of the serration shown in Fig. 9c. The spatial resolution for the wake measurement in the y-direction is typically 0.25 mm in order to capture the large velocity gradient in the viscous sublayer region. The resolution in the z-direction is 0.33 mm for a total distance of 9.9 mm, which is equal to 3λ. As explained earlier in Sect. 2.2, the three velocity components u, v, and w are measured by the X-wire in a two-step approach. The same approach is also adopted in the flow measurements conducted in the streamwise direction, as depicted in Fig. 9d. Note that this measurement accounts for the wake deflection by the cambered aerofoil, i.e. the traversing in the streamwise direction is subjected to a gradient of $dy/dx' = -0.24$.

Note that the above flow measurements were carried out at exactly the same flow condition as the noise tests: $U_\infty = 24\,\mathrm{ms}^{-1}$ and geometrical angle of attack $\theta = 0°$. Three baseline trailing edges ($B\phi_N10$, $B\phi0$ and $B\phi_P10$) are investigated against the three serrated trailing edges ($S\phi_N10$, $S\phi0$ and $S\phi_P10$).

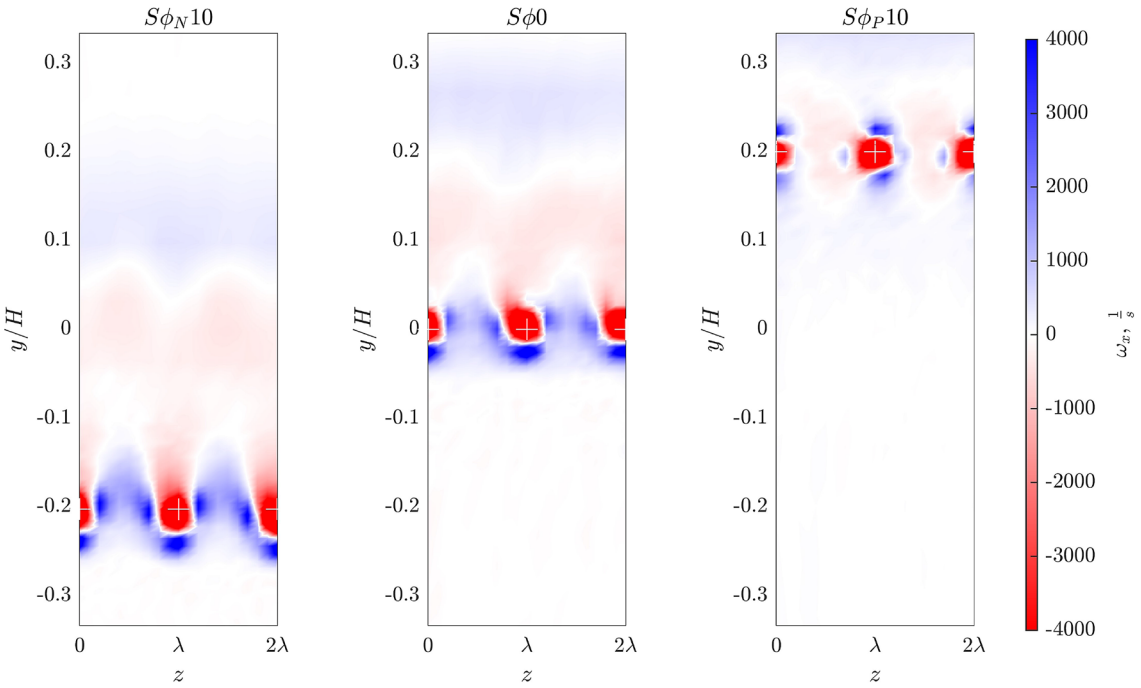

Fig. 12 Streamwise vorticity (ω_x) contour maps in the y/H-z plane at $x' = 1$ mm produced by the $S\phi_N10$, $S\phi0$ and $S\phi_P10$ serrated trailing edges at $U_\infty = 24\,\mathrm{ms}^{-1}$ and $\theta = 0°$. The serration tips are illustrated by the (+)

The results shown in Fig. 10 correspond to the boundary layer measurements upstream of the trailing edges. Figure 10a shows the boundary layer mean velocity profiles at the suction and pressure surfaces for the baseline in $B\phi_N10$, $B\phi0$ and $B\phi_P10$. Note that the freestream velocity U_∞ is taken as the velocity measured at the largest y location away from the aerofoil surface (~ 25.5 mm), which is close to $du/dy = 0$. Boundary layer thickness developed at the pressure surface is considerably larger than that developed at the suction surface. This is due to the designation of NACA 65(12)-10 as a laminar aerofoil, where the highest point at the suction surface occurs at a considerable distance downstream of the leading edge. Therefore, the growth of boundary layer on the suction surface is predominantly subjected to a favourable pressure gradient over more than half chord length of the aerofoil, before slowly diffuses towards the trailing edge under an adverse pressure gradient. On the other hand, the aerofoil pressure surface is largely flat and diverges. The entire surface is predominantly subjected to adverse pressure gradient so the boundary layer has already grown considerably by the time it reaches the trailing edge. In addition, it has also been observed that leading edge separation bubble will be produced upstream of the tripping devices (Chong et al. 2018). The presence of a leading edge separation bubble on the pressure surface will certainly be another factor to increase the overall thickness of the turbulent boundary layer at the trailing edge.

When a negative flap angle is used for the baseline flat plate ($B\phi_N10$), the boundary layer at the suction surface becomes fuller, and even the $u(y)/U_\infty$ at $3 \le y \le 19$ mm has been found to exceed unity. This means that the velocity at this region is higher than the freestream value, suggesting the presence of a near-wall flow acceleration. The boundary layer thickness is also thinner than that produced by the non-flap trailing edge ($B\phi0$). By examining the profile at the pressure surface of the same flap angle ($B\phi_N10$), the boundary layer becomes less full and it is clearly thicker than that produced by the $B\phi0$. These observations can be corroborated to the corresponding turbulent velocity profiles in Fig. 10b. Comparing the $B\phi_N10$ to the $B\phi0$, the turbulence intensity across the thinner boundary layer at the suction surface becomes lower, while the turbulence intensity across the thicker boundary layer at the pressure surface becomes larger. This means that deploying a flap-down to the baseline flat plate will enhance the downwash to achieve stabilisation of the boundary layer near the trailing edge at the suction surface, while it will increase the turbulence characteristics at the pressure surface near the trailing edge.

When a positive flap angle is used ($B\phi_P10$), a completely opposite trend can be observed. Comparing the $B\phi_P10$ to the $B\phi_0$ for the mean and turbulent velocity profiles, a flap-up configuration is shown to thicken the boundary layer and increase the overall turbulence intensity at the suction surface. On the other hand, the boundary layer at the pressure

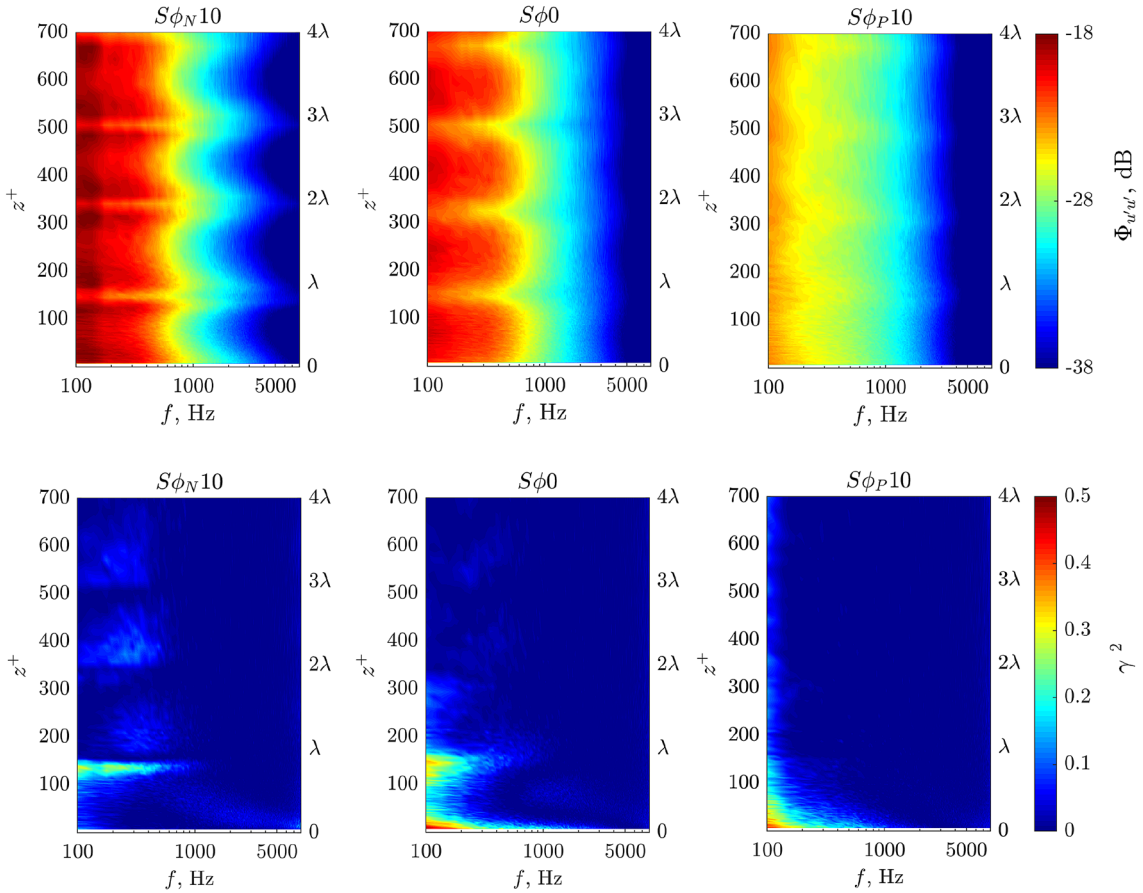

Fig. 13 (Top row) Spanwise distribution of the near wake power spectral density (PSD) of the fluctuating velocity $\Phi_{u'u'}$, dB, and (bottom row) spanwise coherence function γ^2, for the $S\phi_N10$, $S\phi0$ and $S\phi_P10$ serrated trailing edges. All the contours are acquired at $x' = 1$ mm and $y = 0$, under flow condition of $U_\infty = 24\,\mathrm{ms}^{-1}$ and $\theta = 0°$

surface becomes thinner and the overall turbulence intensity is lower.

The analysis now focuses on the comparison between the straight baseline flat plates and serrated flat plates of different flap angles. The comparison is based upon the premise that any changes in the boundary layer velocity profile for a serrated trailing edge can be solely attributed to the sawtooth serration effect. As shown in Fig. 11a for the suction surface, the near-wall acceleration previously observed in the ($B\phi_N10$) disappears considerably for the ($S\phi_N10$). This implies that the stabilising effect of the flap-down configuration has been weakened by the presence of interstices in the serrated flat plate. A similar trend of the serrated velocity profile becoming less full than its baseline counterpart at the suction surface is also demonstrated when comparing the $S\phi0$ against $B\phi0$. However, the boundary layer profiles for both the ($B\phi_P10$) and ($S\phi_P10$) do not exhibit significant difference with each other.

In Fig. 11b for the ($B\phi_P10$) and ($S\phi_P10$) at the pressure surface, the boundary layer profiles between them again do not exhibit significant difference. However, in what previously considered as detrimental to the stability of the boundary layer on the suction surface, the serration now exerts a more stabilising effect on the pressure surface when the flap angle is increasingly deflected downward. Therefore, both the ($S\phi0$) and ($S\phi_N10$) can cause the boundary layer to become thinner and fuller than the ($B\phi0$) and ($B\phi_N10$), respectively.

To summarise, for a serrated flat plate with $\phi \leq 0°$, the boundary layer will be stabilised at the pressure surface, but de-stabilised at the suction surface. However, at $\phi > 0°$, the boundary layer remains unaffected by the serrated flat plate. This provides a first hint that introducing sawtooth interstices on the flap-down flat plate could enhance the three-dimensionality of the flow field. As will be shown later, the large pressure difference near the trailing edge for the $S\phi_N10$ can force an upward cross-flow (pressure surface to suction surface) within the sawtooth gaps. The mixing between the boundary layer and cross-flow at the suction surface can cause an overall reduction in the momentum, which is reflected by the weakening of the near-wall acceleration in the boundary layer velocity profile (Fig. 11a). The cross-flow as a result of the pressure imbalance

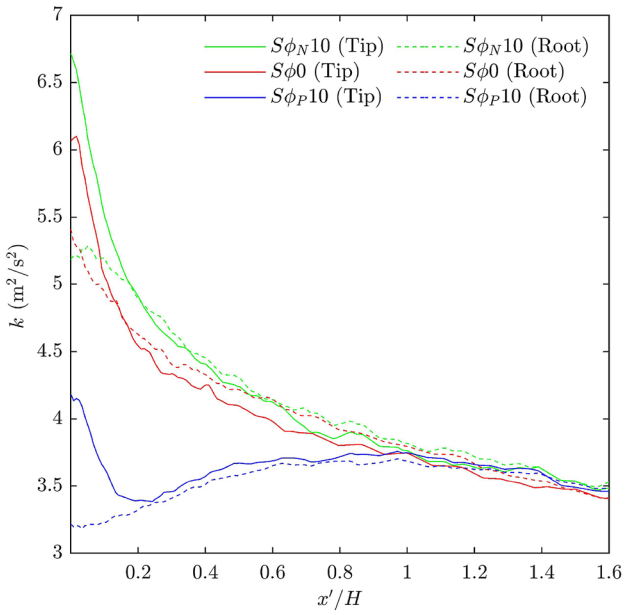

Fig. 14 Streamwise distribution of the serration tip-aligned and root-aligned turbulent kinetic energy k (m/s)^2, produced by the $S\phi_N10$, $S\phi0$ and $S\phi_P10$ serrated trailing edges under flow condition of $U_\infty = 24\,\mathrm{ms}^{-1}$ and $\theta = 0°$

will also drive the boundary layer at the pressure surface of the serrated flat plate to accelerate, resulting in a fuller profile. However, the three-dimensionality of the flow introduced by the serration becomes less obvious when the ϕ is sufficiently positive. This is manifested by the similar boundary layer profiles between the $B\phi_P10$ and $S\phi_P10$ configurations.

The characteristics of the cross-flow mentioned earlier and its influence on the aeroacoustics behaviours of the serrated trailing edges will be investigated from the near-wake flow field. The streamwise vorticity contour maps in the $y-z$ plane at $x' = 1$ mm for the $S\phi_N10$, $S\phi0$ and $S\phi_P10$, measured in accordance with the schematic in Fig. 9c, are shown in Fig. 12. The streamwise vorticity, ω_x, is defined as:

$$\omega_x = \frac{\partial w}{\partial y} - \frac{\partial v}{\partial z}. \tag{7}$$

From the measured data for a baseline straight trailing edge, the $\frac{\partial v}{\partial z}$ term in Equation (7) should be predominantly zero in the near wake. However, there is variation in the spanwise flow components w as a function of y in the near wake. Although not presented here, the near wake pertaining to a baseline straight trailing edge aerofoil will feature alternating signs of ω_x on the suction and pressure surfaces, respectively. The results in Fig. 12 for the serrated trailing edges corroborate well with the earlier conjecture of an upward cross-flow at the sawtooth gaps when $\phi \leq 0°$. For the $S\phi0$ case, the components of the $+\omega_x$ that are otherwise confined at the pressure surface will now be swept and engulfed by the cross-flow and penetrate into the suction surface. This encroachment becomes more prominent for the $S\phi_N10$ case, where the strength of the cross-flow is expected to be stronger. By contrast, the lack of cross-flow component at the sawtooth gaps for the $S\phi_P10$ is manifested by the isolation and localisation of various ω_x components at their respective regions.

The distance in the spanwise direction z in Fig. 13 for the near wake power spectral density (PSD) and coherence spectra γ^2 of the fluctuating velocity will be normalised by the friction velocity u_τ and kinematic viscocity ν in the form of $z^+ = zu_\tau/\nu$, which can represent the wall unit/coordinate. This is because it is widely established that the near wall region of the turbulent boundary layer is populated by hairpin vortices whose legs are stretched along the wall. They are responsible for the low-speed streaks observed in many studies (e.g. Kline et al. (1967), Kim et al. (1971) and Head and Bandyopadhyay (1981)). The average spanwise spacing between the low-speed streaks is known to be approximately $z^+ \approx 100$ (Kline et al. 1967).

Some interesting results can be extracted from the near wake PSD of the fluctuating velocity, as a function of both z^+ and λ, at $x' = 1$ mm and $y = 0$ in Fig. 13 (top row). The schematic explaining the measurement method is shown in Fig. 9b. $z = 0$ corresponds to the location of the "stationary" probe that coincides with the first sawtooth tip (z_o). Therefore, all the data presented in Fig.13 (top row) are measured by the "traversing" probe only. Although not shown here, readers can refer to Fig. 12 in Vathylakis et al. (2016) for the PSD contours corresponding to the baseline trailing edges $B\phi_N10$, $B\phi0$ and $B\phi_P10$. They all exhibit a largely similar spectral behaviours in the near-wake across the same range in z. However, for the serrations $S\phi_N10$ and $S\phi0$, clear periodic patterns of high PSD level are manifested at $0.1 < f < 1.5$ kHz in Fig. 13 (top row). In what follows, the term "large-scale turbulence" will be used to represent the high PSD level in this frequency range.

For the $S\phi0$ case, the periodicity resembles a repeating "∩" shape, each of which is embedded in the region between two consecutive sawtooth tips. In other words, no obvious large-scale turbulence is emanating from the sawtooth tip, while the maximum large-scale turbulence level is achieved at the location aligning with the sawtooth root (i.e. $z = n\lambda/2$, where $n = 1, 3, 5, ...$). For the flap down $S\phi_N10$, the periodicity pattern changes to a repeating "M" shape, where each "M" is also embedded in the region between two consecutive sawtooth tips. Similarly, there is no obvious large-scale turbulence level emanating from the sawtooth tip. However, the maximum large-scale turbulence now shifts to a new location aligning with the middle point of the sawtooth oblique edge, i.e. at z location between the sawtooth tip and root ($z = n\lambda/4$, where $n = 1, 3, 5, ...$). It is now clear that the large-scale turbulence structure is transported by the cross-flow within the sawtooth gaps, as observed in the ω_x contour presented earlier. Deploying a flap-down of the serration flat plate compared to the $S\phi0$ case alters slightly the structure and level of the large-scale

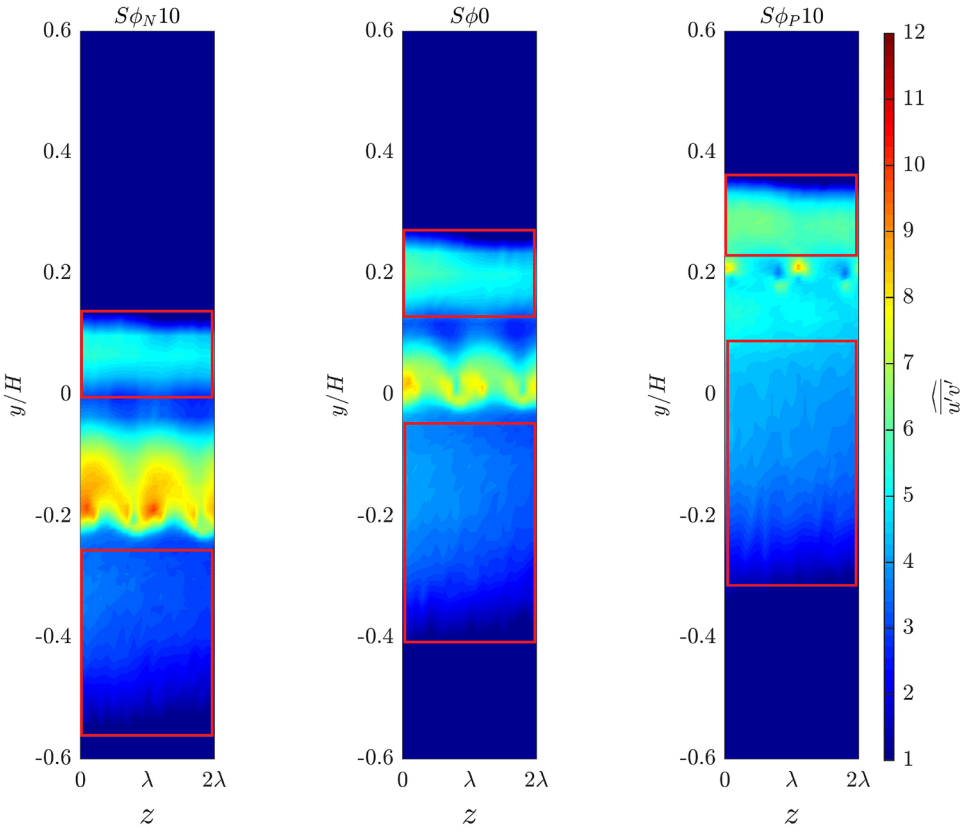

Fig. 15 Comparison of the contour maps of the band-filtered Reynolds shear stresses $\overline{u'v'}$ (m/s)^2 produced by the $S\phi_N10$, $S\phi0$ and $S\phi_P10$ serrated trailing edges at $x' = 1$ mm under flow condition of $U_\infty = 24\,\mathrm{ms}^{-1}$ and $\theta = 0°$

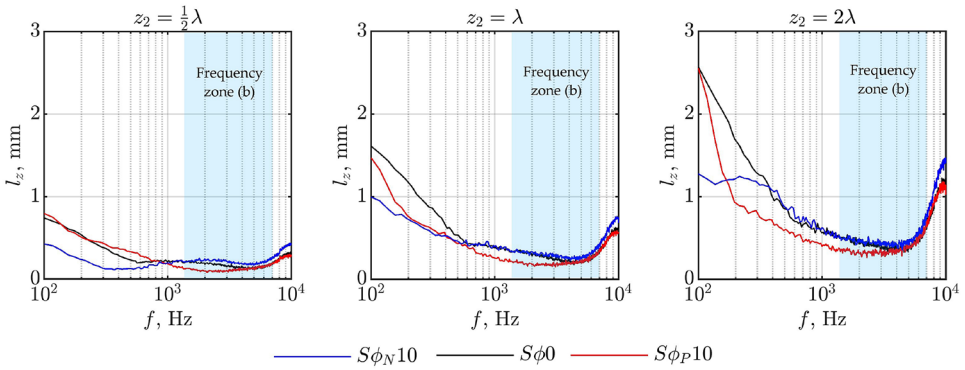

Fig. 16 Comparison of the spanwise correlation length scale l_z mm, produced by the $S\phi_N10$, $S\phi0$ and $S\phi_P10$ serrated trailing edges at $x' = 1$ mm under flow condition of $U_\infty = 24\,\mathrm{ms}^{-1}$ and $\theta = 0°$

turbulence, but the fundamental remains the same. However, for a flap-up serration, i.e. the $S\phi_P10$ case, the large-scale turbulence structure would completely disappear.

The investigation next focuses on the effect of the large-scale turbulence structure on the spanwise coherence spectra $\gamma^2(z,f)$, as shown in Fig. 13 (bottom row). As a reminder, the reference probe aligns with one of the serration tips, where it is designated as $z = 0$ or z_o. For the $S\phi_N10$, before the "traversing" probe reaches the next sawtooth tip, it becomes clear that $\gamma^2 \approx 0$ within the sawtooth gap at $z^+ < 100$. This is expected as the local strong cross-flow would cut-off and eliminate the spanwise coherence that is associated with the turbulent boundary layer, and the fact that the large-scale turbulence has no significant footprint at the sawtooth tip. At the spanwise location around the sawtooth tip at $z^+ \approx$ 130 to 150, however, a relatively high level of γ^2 extending

slightly beyond 1 kHz can be observed. It is important to state at this point that the high coherence observed at $z^+ \approx$ 130 to 150 is not entirely stem from an undisturbed turbulent boundary layer,[1] which is usually associated with a wall-unit of about 100. Instead, the result in the γ^2 contour suggests that a stretched horseshoe-type vortical structure, with the spanwise distance between the two legs of $\approx 130-150$ wall-unit apart, is produced as a response to the presence of the cross-flow within the sawtooth gaps.

For the case of $S\phi 0$, the characteristic of γ^2 described in the previous paragraph becomes less distinct. The transition from an "M" shape to an "∩" shape ($S\phi_N 10 \rightarrow S\phi 0$) in the PSD contours means that the spatial extent for the "cutting-off" of the turbulent boundary layer spanwise coherence by the cross-flow has shifted from the sawtooth mid-point to the sawtooth root region only. As a result, we can observe a relatively strong value of γ^2 between the sawtooth tip and mid-point that is previously unseen in the $S\phi_N 10$ case. It is likely that this recognisable level of spanwise coherence is related to the turbulent boundary layer. On the other hand, the dominant γ^2 at the consecutive sawtooth tips become broadened in the z^+ domain. This may imply a change of the structural characteristics of the horseshoe vortices. Interestingly, the high level of γ^2 at the consecutive sawtooth tip shares a similar frequency range as the frequency zone (a) described earlier for the $\Delta\mathrm{PWL}_s$ in Fig. 6. This observation will be discussed further later.

Finally, the absence of the cross-flow for the $S\phi_P 10$ case contributes to (1) appearance of a γ^2 contour in the $(z-f)$ domain that one would expect from a conventional turbulent boundary layer, and (2) absence of high γ^2 value at the consecutive sawtooth tip. These observations indicate that there is no activity of the horseshoe-like structure convecting pass the serrations at $S\phi_P 10$.

The establishment of the causal effect between the cross-flow (within the sawtooth gaps) and stretched horseshoe vortices (emanated from the sawtooth tips) can be further examined from the turbulent kinetic energy (k) fields aligning to the serration root and tip, respectively. The k, which represents the total kinetic energy of the turbulent fluids taking into account of the three-dimensional velocity fluctuations, is defined as:

$$k = \frac{1}{2}\left(\overline{(u')^2} + \overline{(v')^2} + \overline{(w')^2}\right). \tag{8}$$

The streamwise development of k for the $S\phi_N 10$, $S\phi 0$ and $S\phi_P 10$ serrated trailing edges is shown in Fig. 14. Note that all the distributions of k in the figure are subjected to a universal gradient of $dy/dx' =$-0.24 to account for the wake deflection by the aerofoil camber effect. Several interesting features can be derived from the figure. First, the k at the very near-wake produced by the sawtooth tip, typically at $x'/H < 0.07$, is always larger than that produced by the sawtooth root. The k generated at the sawtooth tip, especially for both the $S\phi_N 10$ and $S\phi 0$ cases, is likely to be associated with the stretched horseshoe vortices. Second, these large level of k at the sawtooth tip will undergo a rapid turbulence decay to eventually collapse to the same k values produced by the sawtooth root, typically after $x'/H \approx 0.1-0.2$. This indicates that a relatively homogeneous turbulent wake can be quickly established despite a highly imbalance of turbulent kinetic energy at the very near-wake. Third, while the $\frac{dk}{dx'}$ produced by the $S\phi_N 10$ and $S\phi 0$ exhibit reasonably similar decay rates between them, the $S\phi_P 10$ is marked by a growth for the k ($\frac{dk}{dx'} > 0$) between $0.2 < x'/H < 1.0$. Within this region, the overall k level for the flap-up serration is also the lowest amongst the configurations considered here. These observations suggest that the main source of the wake turbulent kinetic energy originates neither from the sawtooth tip nor the root for the flap-up configuration, and most interestingly, the weakened turbulent wake could be linked to the better noise reduction performance $\Delta\mathrm{PWL}_S$ at $1.5 < f < 7$ kHz (frequency zone (b) in Fig. 6) by the $S\phi_P 10$. This conjecture can be verified by the investigation of the frequency-filtered power spectral density of the turbulent velocities.

Figure 15 presents the band-filtered Reynolds shear stress in the $y/H - z$ plane, which is defined below:

$$\widehat{\overline{u'v'}}(y/H, z) = \int_{f_1}^{f_2} \psi_{(u'v')}(y/H, z, f)\, df, \tag{9}$$

where the $\psi_{(u'v')}(y/H, z, f)$ is the power spectral density of the Reynolds shear stress $\overline{u'v'}$. f_1 and f_2 are 1.5 and 7 kHz, respectively. This particular frequency range is chosen to coincide with the frequency zone (b) in Fig. 6. It is clear that the amplitude and spatial distribution of the $\widehat{\overline{u'v'}}$ sources surrounding the sawtooth region are the largest for the $S\phi_N 10$. However, deflecting the serrated trailing edge upwards, i.e. increases the ϕ, can reduce the $\widehat{\overline{u'v'}}$ level. The $S\phi_P 10$ represents the configuration that is capable of achieving the largest reduction in the turbulent boundary layer sources surrounding the sawtooth edge, which could explain the best noise reduction performance by this particular configuration at frequency zone (b) in Fig. 6. The overall distributions of the $\widehat{\overline{u'v'}}$ also reflect that whenever significant turbulent sources are amalgamated around the sawtooth region, such as the $S\phi_N 10$ case, the level of $\widehat{\overline{u'v'}}$ at elsewhere within the wake (i.e. the regions within the red boxes) becomes less pronounced. While the $S\phi 0$ continues with the trend, the $S\phi_P 10$ produces an opposite effect where the diminished

[1] Although not shown here, readers can refer to Fig. 12 from Vathylakis et al. (2016), where the corresponding $B\phi_N 10$ only exhibits meaningful level of spanwise γ^2 up to $z \approx 1$ mm.

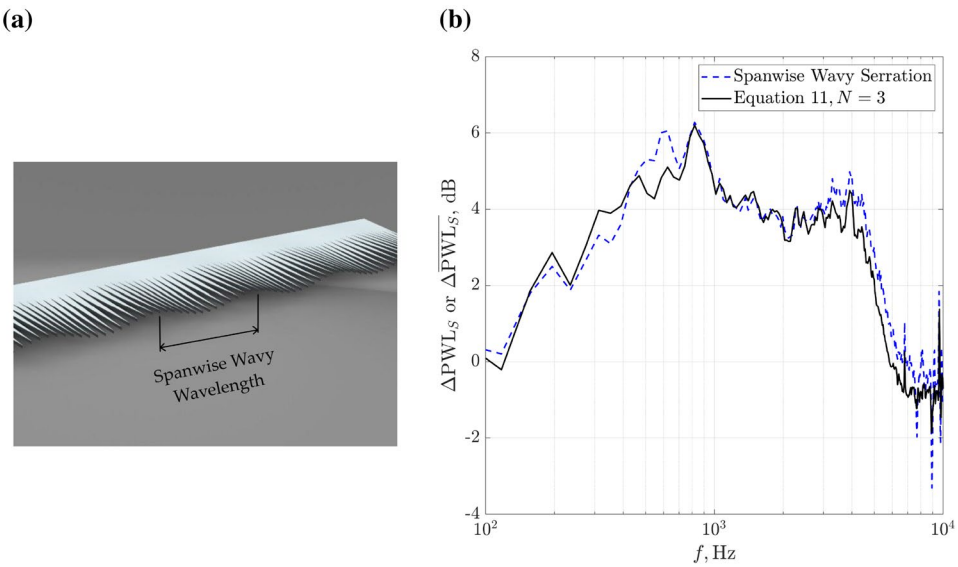

Fig. 17 **a** Schematic illustrating a spanwise wavy serration trailing edge, **b** Comparison of the ΔPWL_S, dB produced by a spanwise wavy serrated trailing edge ($|\phi(z)|_{(\max)} = 5°$) and by Equation (11), $N = 3$ at $U_\infty = 24\,\text{ms}^{-1}$ and $\theta = 0°$

and fragmented $\widehat{u'v'}$ surrounding the sawtooth edge is now accompanied by a relatively larger level of $\widehat{u'v'}$ within the wake regions highlighted by the red boxes. This suggests that a re-distribution of the turbulent sources could be one of the reasons that enables the $S\phi_P10$ to outperform the $S\phi0$ in the noise reduction performance at $f_1 \leq f \leq f_2$. Note that performing the same analysis for the Reynolds normal stress in $\widehat{v'v'}$ will produce the same characteristics as the $\widehat{u'v'}$.

According to Amiet (1976), the spanwise correlation length scale as a function of frequency, $l_z(f)$ represents another main source for the radiation of aerofoil self-noise to the far field. The $l_z(f)$ originates from the coherence function γ^2 in the following form:

$$l_z(f) = \int_{z_1}^{z_2} \sqrt{\gamma^2(z,f)}\, dz \tag{10}$$

where z_1 is the closest spanwise separation distance between the "stationary" and "traversing" probes, and by definition, $z_2 \longrightarrow \infty$. In practice, the γ^2 in the spanwise direction for a turbulent boundary layer would decay quite rapidly to zero especially for the central and high frequencies. Therefore, a low value of z_2 will normally be sufficient. In the current analysis, the z_2 is varied from $\frac{1}{2}\lambda$ to λ, then 2λ, where λ is the serration wavelength. The reason to have different values of z_2 is to examine the sensitivity of l_z in the presence of cross-flow at $\frac{1}{2}\lambda$ and beyond. The results are shown in Fig. 16. The analysis will focus on the frequency zone (b), where $f_1 \leq f \leq f_2$. It can be seen that, contrary to an earlier observation that the cross-flow represents a favourable mechanism to cut-off the large-scale turbulence at low-frequency (frequency zone a), the absence of it for the $S\phi_P10$ serrated trailing edge can actually help to produce a lower value of $l_z(f_1 \leq f \leq f_2)$ as early as when $z_2 = \frac{1}{2}\lambda$. This beneficial effect continues to replicate at $z_2 = \lambda, 2\lambda$ and so on. The results thus suggest that, over a frequency range of interest (i.e. in frequency zone b), a flap-up serration at the trailing edge can produce a better noise reduction performance owing to the weakening of both the turbulence source and spanwise correlation length scale.

4 Discussion of the noise mechanisms

By adding a straight, non-serrated flat plate to the trailing edge of an aerofoil, it is already sufficient to reduce the radiated self-noise at the central frequency region. If the flat plate is longer in length, the level of noise reduction will also be higher. It is likely that the underlying mechanism is related to the "blade-loading" effect, where the turbulent boundary layers near the trailing edge are altered. However, there is a practical limit of how long the add-on straight flat plate can be realistically achieved. Instead, creating interstices in the form of sawtooth serration on the flat plate, one could create an additional"serration" effect that is so reliable to reduce the self-noise that it has been studied extensively in the research community since the last decade. It is worth mentioning that in those studies, the attention is almost exclusively focused on the serration amplitude and serration wavelength only. These are traditionally regarded as the primary geometrical variables for a serration.

The broadband noise reduction by adding a serrated flat plate to the trailing edge of an aerofoil is contributed cumulatively by both the blade-loading and serration effects.

However, the weighting of these two effects in their contributions to the self-noise reduction can also be manipulated by a third serration geometrical parameter, namely the serration flap angle. For example, results presented in this study demonstrate that a supposedly positive blade-loading effect of extending the flat plate length can be negated significantly by a flap-down angle. Therefore, though relatively less studied, the geometrical characteristics of the flap angle can provide a unique opportunity to investigate further the mechanisms of the broadband self-noise reduction by a serrated trailing edge.

For a non-flap serrated trailing edge presented in this paper, the streamwise vorticity plane at the near wake demonstrates that some dominant streamwise vortical components that are otherwise confined at the pressure surface will be swept and engulfed onto the suction surface by cross-flow through the sawtooth gaps. This pressure-driven mechanism corroborates with Avallone et al. (2016), who reported that the flow pattern pertaining to a serrated trailing edge is characterised by pairs of counter-rotating streamwise-oriented vortical structures in the space between the serrations. These structures act to distort the mean flow which, according to Chong and Vathylakis (2015), cause a local variation in the effective angle seen by the turbulent flow approaching the serration edges. The encroachment of the pressure-driven streamwise vortices can compartmentalise the turbulent boundary layer and reduce the level of the spanwise coherence. In addition, it can also force the formation of the stretched horseshoe vortices with the two legs on the consecutive sawtooth tips separated apart by $130 - 150$ wall unit. Clearly, there seems to be a destructive mechanism introduced by the cross-flow. However, further investigation is needed to correlate the frequency range of the radiated far field that is susceptible to the cross-flow.

For the flap-up serrated trailing edges, the lack of cross-flow in the space between the serrations is accompanied by a significant deterioration in the noise reduction performance at low-frequency, which is represented by the frequency zone a defined in Fig. 6b. This provides a clue that the cross-flow is responsible for the noise reduction at low-frequency. This is consistent with the earlier observation of strong perturbations to the large-scale turbulence structures by the cross-flow. It is necessary to point out that the aforementioned blade-loading effect is not prevalent for the flap-up serration based on two experimental evidences. First, the $\Delta\mathrm{PWL}_B$ is zero across a large frequency range (Fig. 8). Second, the turbulent boundary layers just upstream of the flap-up serration remain the same profile between the straight and serrated flat plates (Fig. 11). However, the opposite is observed for the flap-down serration, where the negative blade-loading effect is prevalent. For this very reason, a strong performance in the noise reduction at low-frequency that is otherwise anticipated owing to the presence of the strong cross-flow cannot be realised for the flap-down serration. In fact, the negative blade-loading effect for a flap-down serration is so dominant that the $\Delta\mathrm{PWL}_S$ spectra would start to drop across the entire frequency range as soon as a negative flap angle for the serration is introduced (Fig. 6a).

The absence of cross-flow by the flap-up serration has no detrimental effect on the central-frequency (zone b), as shown in Fig. 6b. It shows that the flap-up serration can outperform the non-flap counterpart within this wide frequency range, while the flap-down serration continues to experience a deterioration in the performance. This is an exciting result and a potential step up for the serration technology—aeroacoustically speaking. The strong performance by the flap-up serration is underpinned by the enhancement of the serration effect through the weakening and re-distribution of the turbulence source around the sawtooth region, and the reduction in the spanwise correlation length scale.

At the high-frequency (zone c) for the non-flap serration, the cross-flow is shown to be a detrimental source owing to its tendency to interact with the sawtooth structure and cause a noise increase. Understandably, the lack of cross-flow for the flap-up serration can avoid the generation of this high-frequency extraneous noise altogether. On the other hand, the flap-down serration continues to be besieged by the negative blade-loading effect and is exacerbated by the very strong cross-flow at the space between the serrations that significant high-frequency noise increase becomes inevitable.

It is worth mentioning that this paper only concerns the effect of serration flap angle to the aeroacoustics performance. For future research, one avenue is to include the effect of the angle of attack. The rationale is that the aeroacoustics comparison could be performed under a condition where the serrated aerofoil with serration flap angle produces the same aerodynamic lift as the serrated aerofoil with zero flap angle.

5 Outlook

In summary, the level of impact by the blade-loading on the serrated flat plate is a function of the flap angle ϕ. This property can be further exploited by varying the ϕ as a periodic function in the spanwise distance z. In addition, the $|\phi(z)|_{(\max)}$ (i.e. maximum values of ϕ_N and ϕ_P) will be the same. A sample of this configuration, which is herein called the "spanwise wavy serration", is illustrated in Fig. 17a. It is hypothesised that the spanwise wavy serration might be able to neutralise the blade-loading effect on the acoustic radiation at the low-frequency region.

As a preliminary study, a spanwise wavy serration of $|\phi(z)|_{(\max)} = 5°$, and a spanwise wavy wavelength of 45 mm (i.e. 30% of the chord), is constructed. The corresponding $\Delta\mathrm{PWL}_S$ produced by this particular spanwise wavy serration is plotted in Fig. 17b. Also included in the figure is the $\Delta\overline{\mathrm{PWL}_S}$, which is defined as:

$$\Delta\overline{\mathrm{PWL}_S} = \left[\sum_{n=1}^{N} \Delta\mathrm{PWL}_{S\cdot n}\right].(N)^{-1}. \tag{11}$$

The $\Delta\overline{\mathrm{PWL}_S}$ thus represents the mean sound power reduction level, as a function of frequency. In the current context, the spectrum is averaged by several serrated flat plates at $|\phi(z)| \leq 5°$, which is $N = 3$ (i.e. $S\phi_N5$, $S\phi0$ and $S\phi_P5$). Figure 17b shows that the noise reduction level produced by the spanwise wavy serration and the $\Delta\overline{\mathrm{PWL}_S}$ are similar at $f < 3$ kHz. This demonstrates that facilitating a spanwise periodicity of the serration flap angle can indeed neutralise the blade-loading effect on the aeroacoustics radiation. On the other hand, at the central and higher frequencies, the spanwise wavy serration outperforms the $\Delta\overline{\mathrm{PWL}_S}$ by up to 1 dB. The same positive outcome also holds true if the spanwise wavy serration is compared directly to the non-flapped $S\phi0$. The results suggest that the turbulence conditioning exerted by the flap-up serration components remains effective and is not negated by the presence of the flap-down serration components in the spanwise wavy configuration.

Although not tested here, the spanwise wavy serration could also produce a similar aerodynamic performance as the non-flapped $S\phi0$. Further investigation is needed to fully establish the potential of this innovative serration configuration.

6 Conclusions

This experimental study investigates the effect of serration flap angle on the aerofoil self-noise radiation. Both the far-field and near-field measurements of a NACA 65(12)-10 were conducted at the Brunel aeroacoustics facility, under a Reynolds number of about 2.96×10^5 and zero degree angle of attack. The serrated flat plate trailing edges were manufactured to cover a range of serration flap-down angles (−15°, −10°, −5°) and flap-up angles (+5°, +10°, +15°), including the 0° representing the reference, non-flap angle.

Using a long serrated trailing edge flat plate at a non-flap configuration, noise reduction can be achieved between the low and central frequencies, but at the high-frequency, noise increase is observed. When a flap-down serration is deployed, the dominant mechanism of the blade-loading will deteriorate the noise reduction performance across almost the entire frequency range. However, when the serrated flat plate is deployed flap-up, noise manipulations at the three frequency zones (low, central and high) are exerted differently despite the disappearance of the blade-loading effect. At the low-frequency zone, the lack of cross-flow mechanism to eliminate the large-scale turbulence would negate the serration effect and cause a significant loss in the noise reduction performance. At the central-frequency zone, however, the weakening and re-distribution of the turbulence source around the sawtooth region, and the reduction in the spanwise correlation length scale, represent the two mechanisms that ultimately improve the noise reduction performance over the conventional non-flap serrated configuration. The lack of cross-flow for the flap-up serration, understandably, switches role to become a positive factor at the high-frequency zone as demonstrated by the lack of noise increase. This is due to the reduced level of interaction between the cross-flow and sawtooth structure. This paper provides a positive outlook of facilitating flap angles to the trailing edge serration in the form of "spanwise wavy serration". This new concept can preserve the noise reduction capability at low-frequency, while improve the noise reduction capability at the central and high-frequency regions.

Acknowledgements This work is supported by the UK Engineering and Physical Sciences Research Council (EPSRC) research grant (EP/N018737/1)"Quiet aerofoils of the next-generation" . We also would like to express our appreciation to the PhD studentships funded by the EPSRC Doctoral Training Partnership (DTP) to the first and fourth authors.

Declarations

Conflict of interest The authors declare that they have no conflict of interest.

References

Acre León C, Ragni D, Pröbsting S, Scarano F (2016) Flow topology and acoustic emissions of trailing edge serrations at incidence. Exp Fluids 57(5):1. https://doi.org/10.1007/s00348-016-2181-1

Amiet RK (1976) Noise due to turbulent flow past a trailing edge. J Sound Vib 47(3):387. https://doi.org/10.1016/0022-460X(76)90948-2

Avallone F, Pröbsting S, Ragni D (2016) Three-dimensional flow field over a trailing-edge serration and implications on broadband noise. Phys Fluids 28(11):117101

Blake WK (1986) Mechanics of Flow-Induced Sound and Vibration, Volume II: Complex Flow-Structure Interaction, 2nd edn. Academic Press. https://www.elsevier.com/books/mechanics-of-flow-induced-sound-and-vibration-volume-2/blake/978-0-12-809274-3

Chong TP, Vathylakis A (2015) On the aeroacoustic and flow structures developed on a flat plate with a serrated sawtooth trailing edge. J Sound Vib 354:65. https://doi.org/10.1016/j.jsv.2015.05.019

Chong TP, Vathylakis A, Joseph PF, Gruber M (2013) Self-noise produced by an airfoil with nonflat plate trailing-edge serrations. AIAA J 51(11):2665. https://doi.org/10.2514/1.J052344

Chong TP, Biedermann T, Koster O, Hasheminejad SM (2018) On the Effect of Leading Edge Serrations on Aerofoil Noise Production. In: 24th AIAA/CEAS Aeroacoustics Conference, AIAA Paper No. 2018-3289. https://doi.org/10.2514/6.2018-3289

Dassen T, Parchen R, Bruggeman J, Hagg F (1996) Results of a wind tunnel study on the reduction of airfoil self-noise by the application of serrated blade trailing edges. In: Proceedings of the European Wind Energy Conference, NLR-TP-1996-350, pp. 800–803. http://hdl.handle.net/10921/1359

Garcia Sagrado AP (2008) Boundary layer and trailing edge noise sources. Ph.D. thesis, University of Cambridge. https://ethos.bl.uk/OrderDetails.do?uin=uk.bl.ethos.612074

Gruber M (2012) Airfoil noise reduction by edge treatments. Phd thesis, University of Southampton. https://eprints.soton.ac.uk/349012/

Gruber M, Joseph PF, Chong TP (2011) On the mechanisms of serrated airfoil trailing edge noise reduction. In: 17th AIAA/CEAS Aeroacoustics Conference, AIAA Paper No. 2011-2781. https://doi.org/10.2514/6.2011-2781

Head MR, Bandyopadhyay P (1981) New aspects of turbulent boundary-layer structure. J Fluid Mech 107:297–338. https://doi.org/10.1017/S0022112081001791

Howe M (1991) Aerodynamic noise of a serrated trailing edge. J Fluids Struct 5(1):33. https://doi.org/10.1016/0889-9746(91)80010-B

Hurault J, Gupta A, Sloth E, Nielsen N, Borgoltz A, Ravetta P (2015) Aeroacoustic wind tunnel experiment for serrated design optimisation and its application to a wind turbine rotor. Int Meet Wind Turbine Noise 39:651–660. https://doi.org/10.1260/0309-524x.39.6.651

Jones LE, Sandberg RD (2012) Acoustic and hydrodynamic analysis of the flow around an aerofoil with trailing-edge serrations. J Fluid Mech 706:295–322. https://doi.org/10.1017/jfm.2012.254

Kim HT, Kline SJ, Reynolds WC (1971) The production of turbulence near a smooth wall in a turbulent boundary layer. J Fluid Mech 50(1):133–160. https://doi.org/10.1017/S0022112071002490

Kline SJ, Reynolds WC, Schraub FA, Runstadler PW (1967) The structure of turbulent boundary layers. J Fluid Mech 30(4):741–773. https://doi.org/10.1017/S0022112067001740

Liu Q, Miao W, Li C, Hao W, Zhu H, Deng Y (2019) Effects of trailing-edge movable flap on aerodynamic performance and noise characteristics of VAWT. Energy 189:116271. https://doi.org/10.1016/j.energy.2019.116271

Moreau DJ, Doolan CJ (2013) Noise-reduction mechanism of a flat-plate serrated trailing edge. AIAA J. 51:2513. https://doi.org/10.2514/1.J052436

Moreau S, Laffay P, Idier A, Atalla N (2016) Several noise controls of the trailing-edge noise of a Controlled-Diffusion airfoil. In: 22nd AIAA/CEAS Aeroacoustics Conference Lyon, France, AIAA 2016-2816 paper. https://doi.org/10.2514/6.2016-2816

Oerlemans S, Fisher M, Maeder T, Kogler K (2009) Reduction of wind turbine noise using optimized airfoils and trailing-edge serrations. AIAA J 47(6):1470. https://doi.org/10.2514/1.38888

Vathylakis A, Chong TP, Paruchuri C, Joseph P (2016) Sensitivity of aerofoil self-noise reductions to serration flap angles. In: 22nd AIAA/CEAS Aeroacoustics Conference, AIAA Paper No. 2016-2837. https://doi.org/10.2514/6.2016-2837

Woodhead PC, Chong TP, Wissink J (2017) Exploiting the Misalignment of the Serrated Trailing Edge for Improved Aerofoil Broadband Noise Reduction. In: 23rd AIAA/CEAS Aeroacoustics Conference, AIAA Paper No. 2017-4175. https://doi.org/10.2514/6.2017-4175. https://arc.aiaa.org/doi/abs/10.2514/6.2017-4175

Zhou P, Liu Q, Zhong S, Fang Y, Zhang X (2020) A study of the effect of serration shape and flexibility on trailing edge noise. Phys Fluids 32(12):127114. https://doi.org/10.1063/5.0032774